TAMPEREEN TEKNILLINEN YLIOPISTO
TAMPERE UNIVERSITY OF TECHNOLOGY

HENRIK ALENIUS

Modeling and Electrical Emulation of Grid Impedance for Stability Studies of Grid-Connected Converters

Master of Science Thesis

Examiners:
Assistant Prof. Tuomas Messo and Academy Research Fellow Tomi Roinila

Examiners and topic approved by the Faculty Council of the Faculty of Computing and Electrical-Engineering on the 27th of October 2017

ABSTRACT

HENRIK ALENIUS: Modeling and Electrical Emulation of Grid Impedance for Stability Studies of Grid-Connected Converters
Tampere University of Technology
Master's Thesis, 67 pages, 3 appendix pages
February 2018
Master's Degree Programme in Electrical Engineering
Major: Power electronics
Examiners: Assistant Prof. Tuomas Messo and Academy Research Fellow Tomi Roinila
Keywords: grid impedance, weak grid, power hardware-in-the-loop, grid-connected converter, impedance-based stability analysis

The access to reliable and affordable energy is vital for a modern society. The climate change and increased consciousness of the environment has shifted the global energy production towards new, renewable alternatives. The rapid growth of renewable energy production increases the amount of grid-connected converters in the power system. However, the dynamics and grid requirements for converters are very different than for conventional rotating generators.

The interface between the converter and grid is prone to stability issues. The stability can be assessed based on the ratio of the inverter output impedance and the grid impedance. However, the grid impedance is often an unknown parameter and modeled based on simplified assumptions. The most common model for the grid impedance is a series connected inductor and resistor. Grid impedance measurements have shown the grid impedance to have more complex, resonant and time-variant characteristics, which are neglected in the conventional modeling approach.

This thesis presents grid impedance models, in which the complex nature of the grid impedance is accurately considered. The enhanced models are based on aggregation of grid elements into sub-models, where the resonant and time-variant behavior is clearly shown. In addition, this work introduces a power hardware-in-the-loop setup for testing a grid-connected inverter in various grid conditions. The derived grid models are applied in a real-time grid simulator, which in turn provides references for a linear amplifier operating as a grid emulator. Thus, a real inverter can be connected to a simulated grid conditions. The versatility and desired behavior of the setup are verified with grid impedance measurements from the grid emulator.

TIIVISTELMÄ

HENRIK ALENIUS: Verkkoimpedanssin mallinnus ja sähköinen emulointi vaihtosuuntaajien stabiiliustarkasteluun
Tampereen teknillinen yliopisto
Diplomityö, 67 sivua, 3 liitesivua
Helmikuu 2018
Sähkötekniikan diplomi-insinöörin tutkinto-ohjelma
Pääaine: Tehoelektroniikka
Tarkastajat: Assistant Prof. Tuomas Messo ja Akatemiatutkija Tomi Roinila
Avainsanat: verkkoimpedanssi, heikko verkko, impedanssi-pohjainen stabiiliusanalyysi, verkkoon kytketty vaihtosuuntaaja

Luotettava ja edullinen sähkönsaanti on yksi nyky-yhteiskuntamme kulmakiviä. Ilmastonmuutos ja kasvanut tietoisuus ympäristöstä ovat muokanneet sähköntuotantoa kohti uusiutuvia energialähteitä, kuten tuuli- ja aurinkoenergiaa. Valtaosa uusiutuvasta sähköntuotannosta kytkeytyy sähköverkkoon vaihtosuuntaajilla, joiden määrä verkossa on kasvanut nopeasti tuuli- ja aurinkosähkön yleistyessä.

Vaihtosuuntaajaan perustuvan verkkorajapinnan dynamiikka ja vaatimukset sähköverkolle poikkeavat suuresti perinteisistä tahti- ja induktiogeneraattoreista. Verkkorajapinnassa esiintyviä stabiiliusongelmia voidaan tutkia vaihtosuuntaajan lähtöimpedanssin ja verkkoimpedanssin suhdeluvun avulla. Verkkoimpedanssi on kuitenkin usein tuntematon muuttuja, jonka mallintaminen perustuu yksinkertaistettuihin oletuksiin. Tavallisin verkkoimpedanssimalli koostuu sarjaankytketyistä induktanssista ja resistanssista. Mittaukset todellisista sähköverkoista ovat osoittaneet sähköverkon impedanssin olevan huomattavasti käytetyimpiä malleja monimutkaisempi.

Tämä diplomityö esittelee menetelmiä monimutkaisen verkkoimpedanssin tarkempaan mallintamiseen. Kehitetyt mallit perustuvat sähköverkkoelementtien koostamiseen alisysteemeiksi, joita hyödyntämällä voidaan mallintaa resonoivia ja aikavariantteja sähköverkkoja. Lisäksi diplomityössä esitellään vaihtosuuntaajan stabiiliustarkasteluun testausjärjestelmä, jossa sähköverkkoemulaattorina toimiva lineaarivahvistin toistaa reaaliaikaisesti simuloituja verkkomalleja. Näin tarkasteltava vaihtosuuntaaja voidaan yhdistää emuloituun sähköverkkoon, ja vaihtosuuntaaja-sähköverkko -rajapintaa voidaan tarkastella monipuolisissa olosuhteissa. Järjestelmän toiminta varmistettiin mittaamalla verkkoemulaattorin impedanssia.

PREFACE

This thesis was carried out in the laboratory of Electrical Energy Engineering at Tampere University of Technology and it concludes my journey towards the Master's degree in Electrical Engineering. However, the Master's thesis turned out to be just a preface for the next part of the journey - the doctoral studies.

I would like to thank my supervisors Assistant Prof. Tuomas Messo and Dr. Tomi Roinila, whose expertise and guidance made this research possible. I owe thanks to the whole power electronics research team, and especially to Jussi, Roni, and Tommi, with whom I shared the office. The atmosphere in our office has been relaxed, focused, and scientific in the exactly right proportions. Not once did I feel reluctant to leave for work in the morning.

I thank my family and friends for their support during the thesis, as the past months have not always been the brightest. Lastly, I want to mention the community of lifting club Herwannan Hauiskääntö, which acted as a counterweight to Academia.

Tampere, 22.1.2018

Henrik Alenius

CONTENTS

LIST OF FIGURES

ABBREVIATIONS AND SYMBOLS

ABBREVIATIONS

AC	Alternating current
DC	Direct current
DG	Distributed generation
DQ-domain	Direct-quadrature -domain
FRA	Frequency response analyzer
HUT	Hardware under test
HV	High voltage
HVDC	High voltage direct current
IGBT	Insulated gate bipolar transistor
LV	Low voltage
MLBS	Maximum-length binary sequence
MV	Medium voltage
NRF	Natural reference frame
p.u.	Per-unit value
PHIL	Power hardware-in-the-loop
PID controller	Proportional-integral-derivative controller
PLL	Phase-locked-loop
PoC	Point of connection
PRBS	Pseudo-random binary sequence
PV	Photovoltaic
RMS value	Root-mean-square value
RTDS	Real-time digital simulator
SCR	Short-circuit ratio
SNR	Signal-to-noise ratio
SRF	Synchronous reference frame
THD	Total harmonic distortion
WG	Wind generators
VSC	Voltage-sourced converter
X/R-ratio	Reactance/resistance -ratio
XOR	Exclusive or -operator

SYMBOLS

α	Alpha component
β	Beta component
ΔI	Change in current
ΔI_o	Output current ripple
Δt	Time step
ΔU	Change in voltage
∞	Infinity
ω	Frequency in radians
ω_{res}	Resonant frequency in radians
ω_{z-CC}	Current controller zero frequency in radians
ω_i	Injection frequency in radians
ω_s	Synchronous frequency in radians
σ	Laplace variable real component
θ_s	Instantaneous angle
$\mathbf{A}$	Coefficient matrix A for state-space representation
$\mathbf{B}$	Coefficient matrix B for state-space representation
$\mathbf{C}$	Coefficient matrix C for state-space representation
$\mathbf{D}$	Coefficient matrix D for state-space representation
$\mathbf{G}$	Transfer function matrix
$\mathbf{I}$	Identity matrix
$\mathbf{T}^{\alpha\beta}$	Clarke's matrix
$\mathbf{T}^{dq}$	Park's matrix
$\mathbf{u}$	Input vector
$\mathbf{U}$	Laplace domain input matrix
$\mathbf{x}$	State vector
$\dot{\mathbf{x}}$	State vector derivative
$\mathbf{y}$	Output vector
$\mathbf{Y}$	Laplace domain output matrix
a	Fortescue's operator
A	Injection amplitude
C	Capacitance
C_{eq}	Equivalent capacitance
C_c	Transmission cable shunt capacitance
C_f	Filter capacitance
C_i	Equivalent inverter capacitance

D_{DG}	Distributed generation transmission line length
D_c	Length of the transmission cable
D_d	Distribution transmission line length
D_u	Upstream transmission line length
d	Differential operator
f_{LC}	LC-resonant frequency
f_{res}	Resonant frequency
f_{sw}	Switching frequency
i_{in}	Input current
I_{Z_s}	Current to source impedance
I_L	Load current
i_o	Output current
I_S	Source current
j	Imaginary unit
K	Scaling factor
K_{CC}	Current controller gain
L	Inductance
L_{eq}	Equivalent inductance
L_{fc}	Filter converter-side inductance
L_{fg}	Filter grid-side inductance
L_{LV}	Inductance of low-voltage line
L_{MV}	Inductance of medium-voltage line
L_c	Transmission cable inductance
P	Active power
R	Resistance
r	Ratio of LCL-filter inductances
R_{eq}	Equivalent resistance
R_{LV}	Resistance of low-voltage line
R_{MW}	Resistance of medium-voltage line
R_C	Transformer core-loss resistance
R_c	Transmission cable resistance
R_d	Damping resistor for capacitor
r_k	Transformer relative resistance
R_K	Transformer series resistance
s	Laplace variable
S_{sc}	Short-circuit power
S_{tf}	Transformer apparent power

S_B	Apparent power base value
S_n	Nominal power
t	Time
u_{in}	Input voltage
U_{LV}	Voltage at the low-voltage side
U_{PoC}	Voltage at the point-of-connection
U_B	Voltage base value
U_g	Grid voltage
U_n	Nominal voltage
u_o	Output voltage
V	Line-to-line voltage
V_{in}	Input voltage
V_L	Load voltage
V_m	Harmonic voltage of order m
X	Reactance
x	Capacitor design constant for LCL-filter
x_k	Transformer relative inductance
X_M	Transformer magnetizing reactance
Y	Admittance
Y_{abc}	Phase domain admittance
Z	Impedance
Z_{abc}	Phase domain impedance
Z_{dd}	Impedance from d-current to d-voltage
Z_{dq}	Cross-coupling impedance from d-current to q-voltage
Z_{eq}	Equivalent impedance
Z_{inv-o}	Inverter output impedance
Z_{PV}	Impedance of the photovoltaic sub-model
Z_{qd}	Cross-coupling impedance from q-current to d-voltage
Z_{qq}	Impedance from q-current to q-voltage
Z_B	Impedance base value
Z_C	Capacitor impedance
Z_d	Impedance of the distribution sub-model
Z_g	Grid impedance
Z_l	Load impedance
Z_L	Inductor impedance
Z_s	Source impedance
Z_u	Impedance of the upstream sub-model

SUB- AND SUPERSCRIPTS

x_-	Negative sequence
x_α	Alpha component
x_β	Beta component
x_+	Positive sequence
x_C	Parameter related to capacitor
x_d	Direct component
x_{dd}	Transfer function from d to d-component
x_{dq}	Transfer function from d to q-component
x_{eq}	Equivalent parameter
x_{in}	Input parameter
x_{ind}	Input d-component
x_{inq}	Input q-component
x_L	Parameter related to inductor
x_o	Output parameter
x_{od}	Output d-component
x_{oq}	Output q-component
x_P	Transformer primary side
x_q	Quadratic component
x_{qd}	Transfer function from d to d-component
x_{qq}	Transfer function from q to q-component
x_R	Parameter related to resistor
x_S	Transformer secondary side
$x^{'}$	Reduced value
$x^{\alpha\beta}$	Alpha-beta -domain
x^{dq}	Direct-quadrature -domain

1. INTRODUCTION

A robust electric power system is one of the headstones of a modern society. However, the means of energy production have experienced a dramatic change during the 21st century, as the climate change imposes new requirements for the energy field. Thus, the role of sustainability and environmental issues has started to grow at an increasing rate. New renewable energy sources provide a sustainable, clean, and efficient solution to the increasing energy demand in the world. During the past decades, renewables like solar and wind power have experienced exponential growth and are slowly challenging the traditional way of producing energy in the combustion power plants.

This trend in renewable energies will continue in the future, as most of the countries are striving for increasing the share of clean energy production. For example, the European Union aims to increase the share of renewable energy to 27 %, in addition to other environmental objectives, by 2030 [1]. Many countries have similar goals for energy production. These efforts promote the increase of renewable energy production capacity.

The majority of renewable energy sources connect to power grid through power electronics, usually three-phase inverters. An inverter transforms the energy from source to suitable form for injection to the power grid. This means modifying the frequency of alternating current (AC) or transformation from direct current (DC) to AC. In addition, power electronics are widely used in all electric systems, including industry, transmission, and consumer electronics. Figure 1.1 illustrates the interconnection of photovoltaic system and power grid. According to [2], in USA roughly 70 % of electricity flows through power electronics, and this share is predicted to eventually increase close to 100 %.

It is well known that grid connected power electronics contribute to adverse phenomena in power grid, including harmonic resonance and possible instability. Many of these adverse effects result from the interaction between the device and grid

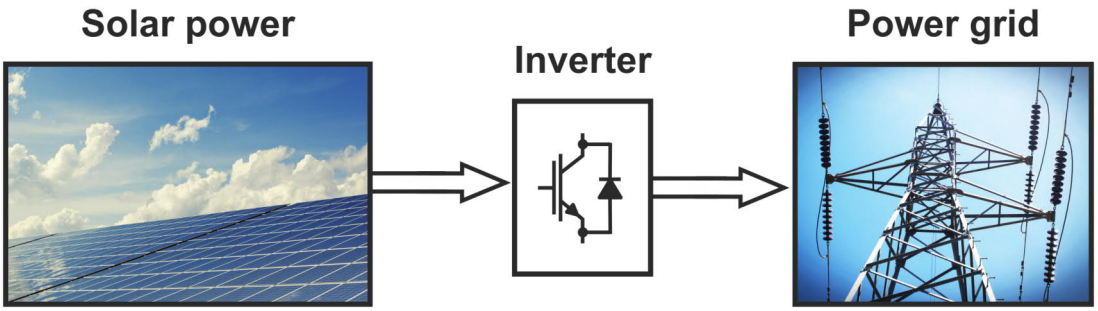

Figure 1.1 *Grid connection of photovoltaic power plant.*

impedance. Due to increasing penetration level of power electronics in the grid, the stability and optimal operation of the devices is of great importance. Consequently, the control and operation of grid-connected converters are well-studied areas. Many different approaches are presented for mitigating the undesired phenomena caused by grid-interaction [3–7]. However, unpredicted instabilities have occurred in converter-dominant systems in large-scale wind and solar plants [8–10].

Adverse interaction with the grid is strongest when the grid conditions are weak, that is, the grid impedance is high [11–15]. The resonance or instability may occur at any frequency, so the complete frequency spectrum should be taken into account, in addition to the fundamental frequency. Therefore, grid impedance of a wide frequency range is a very important design parameter. Information on the frequency-dependent grid impedance is essential for accurate analysis of the grid pollution and instability issues in converters. In this thesis, the grid impedance refers to frequency-dependent grid impedance. Traditional short-circuit analysis provides accurate information on the impedance of power grid only on the fundamental frequency, as the impedance values of transmission lines, transformers, and other grid components are usually known. However, the loads and distributed generation (DG) of the power grid are more difficult to predict and model, and thus the system complexity increases.

The impact of grid impedance to the operation of a grid-connected converter is considered in many publications [11,15–18]. The commonly used grid impedance models are often very simple when analyzing the stability or control of grid-connected converters. In many cases, the grid impedance of a weak grid is modeled as a constant resistance and inductance, typically varying from 1 to 5 mH in low voltage (LV) point of connection [3, 12, 16, 19–22]. Occasionally, higher inductances up to 12.8

mH are used [23].

Although multiple methods for measuring grid impedance have been presented [24–28], accessible measurements on the impedance of real power grids are rare. The work in [29–32] have presented measurement data on the grid impedance from public LV grids. In addition, in [33], grid impedance was measured at HV railroad converter station. These measurements show that grid impedance at distribution grid bus bar consists of impedances of feeding high voltage (HV) upstream grid, distribution grid, and distributed generation.

The measurements on real power grids show different grid impedance patterns compared to commonly used simple impedance models. A simplified RL-model suggests almost linearly increasing impedance magnitude when frequency increases; however, this was not the case in real measurements. Simple models ignore the resonances between the capacitive and inductive elements, which usually occur in frequencies from 250-10000 Hz. These resonances may have dramatic impact on the grid impedance, and hence on the operation of grid-connected converters. In some cases, the resonance may significantly affect the grid impedance phase and magnitude, and thus provoke undesired and unpredicted phenomena. Another important observation from the measured grid impedances is the time variance of the grid impedance. All analyzed measurements observed a strong grid-impedance dependency on the time of the day. Measurements carried out in [30] show that the nighttime resonance may increase the impedance magnitude by 200 % at certain frequencies. On the other hand, the phase can experience up to 50° shift based on time of the day. As a conclusion, it is clearly shown that the simplified grid impedance models neglect some important characteristics of the real grid impedance. In addition, high-frequency grid impedance cannot be derived from short-circuit calculations of grid impedance at fundamental frequency. Thus, in most cases the basic RL-models or network calculations do not describe grid impedance with sufficient accuracy.

Although grid-connected devices and measuring the grid impedance are studied intensively, modeling of the grid impedance is often insufficient or arbitrary. Only few real measurements are performed, and efficient models based on obtained data are lacking. Consequently, accessible and justified grid impedance modeling methods would benefit future research and testing of grid-connected devices. This would ensure the relevance of research results, as the applied grid impedance models would describe the real grid more accurately. Especially in weak grid, the grid impedance is

one of the leading design factors for inverters, and thus the choice of grid impedance model is important.

The purpose of this thesis is to improve the methods for stability assessment of grid-connected converters. The thesis presents a grid impedance modeling approach based on the use of aggregated sub-models, which aims to replace the commonly used arbitrary series inductance models. Three grid scenarios are constructed based on the introduced modeling methods, from which the complex and resonant characteristics of a real power grid are clearly shown. Secondly, thesis introduces a power hardware-in-the-loop (PHIL) setup, where a physical inverter connected to a simulated grid can be analyzed. A linear amplifier is used in the setup to emulate the grid voltage references from a real-time simulator. The operation of the PHIL setup is verified with impedance measurements from the emulation, which are compared to analytical references.

The results show that the introduced methods for grid impedance modeling are capable of accurately describing the complex, resonant and time-variant nature of the real grid. The series and parallel resonances are modeled at correct frequencies, and the impact of time-variant load changes on the grid impedance are presented properly. The measurements from the PHIL emulation show very accurate replication of the simulated grid impedance in the frequency range from 10 to 1000 Hz. The PHIL setup combines the advantages of pure simulations and hardware tests, and therefore is a powerful and cost-effective tool for converter testing. Thus, the enhanced models and PHIL emulation of grid impedances presented in this thesis can improve the stability assessment of grid-connected converters, which in turn enables the further progress in the share of renewable production.

This thesis consists of five chapters. Chapter 2 presents the fundamental mathematical tools for the rest of the thesis, and discusses the interface between the grid and grid-connected converters. Chapter 3 conducts a literature survey on grid impedance in context of power electronics and describes the main grid characteristics. In addition, the grid impedance modeling methods are presented and discussed. Next, Chapter 4 introduces the experimental PHIL setup, which is then verified with simple tests. Three different grid scenarios are emulated based on the models shown in previous chapter, and the emulated impedances are measured. Lastly, Chapter 5 concludes the main findings and experimental results of this thesis.

2. INTERFACE BETWEEN CONVERTER AND GRID

This chapter introduces the theoretical background for analyzing the phenomena in the converter-grid interface. First, mathematical tools for analysis of the operation and stability of the grid-connected inverters are presented, with focus on the impedance-based interactions. Then, the methods for measuring the grid impedance are shown, and the measurement of impedance in the direct-quadrature domain (dq-domain) is discussed.

2.1 Frequency domain and reference frames

Almost all current large-scale power systems are three-phase AC systems. An AC system consists of three sinusoidal phases in 120 degree phase-shift. However, compared to simple DC systems, a three-phase system is more complex so accurate analysis requires sophisticated calculation methods. Although time domain is intuitive and sufficient in many applications, it lacks some features available only in frequency domain.

2.1.1 DQ-domain

A time-domain analysis of sinusoidal, potentially distorted, quantities is possible only for very basic circuits. However, the three phases can be represented as phasors, in which the length corresponds to the amplitude and angle shows the phase-shift. The phases are typically represented using Fortescue's operator a, which equals to 120 degree phase-shift

$$a = e^{j\frac{2\pi}{3}} \tag{2.1}$$

The phasors of the three phases can be transformed to one rotating space-vector in $\alpha\beta 0$-domain using Clarke's transformation. This vector consists of two sinusoidal

signals α and β, as the zero component is negligible in balanced systems, and thus the amount of AC signals decreases from three to two. Transform shows quantities in natural reference frame (NRF) and it is calculated from

$$\begin{bmatrix} x_\alpha(t) \\ x_\beta(t) \\ x_0(t) \end{bmatrix} = \underbrace{K \begin{bmatrix} 1 & -\frac{1}{2} & -\frac{1}{2} \\ 0 & \frac{\sqrt{3}}{2} & -\frac{\sqrt{3}}{2} \\ \frac{1}{2} & \frac{1}{2} & \frac{1}{2} \end{bmatrix}}_{\mathbf{T}^{\alpha\beta}} \begin{bmatrix} x_a(t) \\ x_b(t) \\ x_c(t) \end{bmatrix} \tag{2.2}$$

where $\mathbf{T}^{\alpha\beta}$ is Clarke's matrix in which variable K is the scaling factor. For amplitude invariant system K equals 2/3. However, the AC nature of the rotating vector prevents the use of traditional proportional-integral-derivative controllers (PID controller), which can control only DC error signals to zero.

In order to remove the AC nature of signals, the reference frame can be rotated along the space-vector. This frame is called synchronous reference frame (SRF) in which direct and quadrature components depict the constant space-vector now shown in dq-domain. Multiplying NRF space-vector with a rotating unit vector transforms it into SRF according to

$$\mathbf{x}^{\alpha\beta} = \mathbf{x}^{dq} * e^{j\omega_s t}. \tag{2.3}$$

Thus, the quantities in abc-domain transform directly to dq-domain with Park's matrix

$$\begin{bmatrix} x_d \\ x_q \\ x_0 \end{bmatrix} = \underbrace{\frac{2}{3} \begin{bmatrix} \cos(\theta_s) & \cos(\theta_s - \frac{2\pi}{3}) & \cos(\theta_s - \frac{4\pi}{3}) \\ -\sin(\theta_s) & -\sin(\theta_s - \frac{2\pi}{3}) & -\sin(\theta_s - \frac{4\pi}{3}) \\ \frac{1}{2} & \frac{1}{2} & \frac{1}{2} \end{bmatrix}}_{\mathbf{T}^{dq}} \begin{bmatrix} x_a \\ x_b \\ x_c \end{bmatrix} \tag{2.4}$$

where $\mathbf{T}^{dq}$ is Park's matrix. Again, the zero component is not present in balanced systems. This results in two DC signals, which define the original balanced three phase signals. However, when the equations contain derivatives of quantities, dq-transform introduces cross couplings into system. This happens because of the nature of exponent function derivative

$$\frac{\mathrm{d}(\mathbf{x}^{dq} * e^{j\omega_s t})}{\mathrm{d}t} = \frac{\mathrm{d}(\mathbf{x}^{dq})}{\mathrm{d}t} * e^{j\omega_s t} + j\omega_s \mathbf{x}^{dq} * e^{j\omega_s t} \tag{2.5}$$

contains term $j\omega_s \mathbf{x}^{dq} * e^{j\omega_s t}$ with imaginary unit coefficient, which effectively rotates a space-vector by 90 degrees. In order to solve derivative term from equa-

tion, the cross-coupled term is moved to the other side of the equation and its sign changes. The rotation of space-vector shifts direct quantity to quadrature quantity, and quadrature quantity to negative direct quantity, according to

$$-j * \begin{bmatrix} x^d \\ x^q \end{bmatrix} = \begin{bmatrix} x^q \\ -x^d \end{bmatrix} \tag{2.6}$$

As a result, q-component occurs in equation for d-components and the other way round, and therefore the direct and quadrature components become cross-coupled. Cross-couplings prevent the decoupled analysis of components and hence the model becomes more complex. However, in many cases the cross coupling values are very small compared to d and q-components, and hence can be neglected. [34]

2.1.2 Fourier transform

Most of the analysis for three-phase systems bases on sinusoidal signals. However, often signals are not sinusoidal, especially when analyzing transient or distorted effects. According to Fourier theorem, a signal can be represented as the sum of sine waves at different frequencies. The definition of Fourier transform is

$$F(\omega) = \int_{-\infty}^{\infty} f(t) e^{-2\pi j t} \mathrm{d}t \tag{2.7}$$

As a result, non-sinusoidal effects can be analyzed as sine waves after Fourier transform. Figure 2.1 deconstructs a heavily distorted voltage signal into equivalent frequency components. Harmonic voltages pollute the fundamental frequency voltage of 230 V. The distortion contains sinusoids at 150 Hz, 550 Hz and 1500 Hz with amplitudes of 46 V, 11.5 V and 4.6 V, respectively. All the voltages are root-mean-square (RMS) values.

A Fourier analysis of distorted voltage yields different frequency sinusoids in frequency domain, as shown in Figure 2.2. The height of the bar represents RMS value of voltage at a certain frequency.

2.1.3 Frequency-domain

The analysis of fundamental grid frequency is often enough for conventional power grid inspection. However, a grid-connected converter operates at a wide frequency

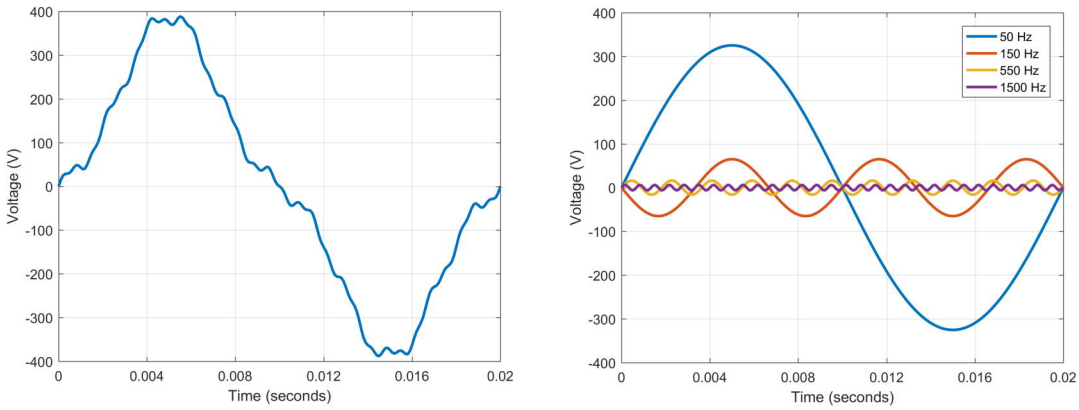

Figure 2.1 *Distorted phase voltage (left) and corresponding deconstructed frequency components (right).*

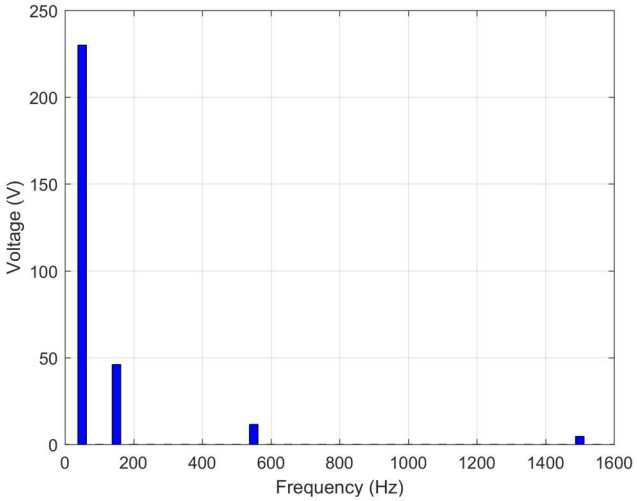

Figure 2.2 *Distorted voltage in frequency domain.*

spectrum and thus simplified analysis with only fundamental frequency is not satisfactory. Analysis of inverters usually takes places in the frequency domain. In frequency domain, the main variable is Laplace variable s, which depicts a complex frequency, instead of time t.

Transformation from time to Laplace domain bases on integral of function times exponential function. This Laplace transform is defined according to equation 2.8

$$F(s) = \int_0^\infty f(t)e^{-st}\mathrm{d}t \tag{2.8}$$

where $f(t)$ is the original time-domain function and s is Laplace variable, $s = \sigma + j\omega$. Frequency domain simplifies some parts of the analysis greatly. For example, time-domain differential equations transform to algebraic equations in frequency domain, which allows significantly easier calculations.

2.2 Grid-connected converters

The amount of distributed generation has soared during the past decade, driven especially by the rapid increase of renewable energy sources. Typically, distributed generation connects to power grid through a power electronics device. Traditional large rotating generators used in MW-scale power production connect directly via magnetic coupling, and thus the increasing use of power electronics reshapes the energy system. The renewable distributed generation consists of mostly wind and solar power. Although wind generators (WG) have a rotating turbine enabling the direct power feed to grid via magnetic coupling, a power-electronic link is often used in between the generated power and the grid feed-in. This enables decoupling of rotational speed of the turbine and grid frequency. In addition, the use of power electronics can remove the need for mechanical transmission, which is a heavy component and prone to failures [35]. On the other hand, photovoltaic (PV) applications convert the energy from solar radiation to DC. In order to feed the DC into the power grid, an inverter is required. As a conclusion, DG generally contains an inverter connected to the grid. Thus, the stability assessment of inverters is vital part of design process of renewable generation systems. The impedance-based interactions between grid and inverter have proven to be an important factor in the harmonics generated by inverters. Realistic grid impedance values are important for increasing the accuracy of impedance-based stability analysis of inverters.

2.2.1 Three-phase inverter dynamics

As the number of inverters connected to grid increases, the design of devices becomes increasingly important for the reliable operation of the power system. A converter design sufficient for ideal grid conditions may turn out to be unsuitable for a real grid, which contains harmonic currents and voltages, transients, and non-zero grid impedance. The dynamic behavior of the inverter must be known for stable operation with good power quality. Therefore, an advanced model of inverter is required

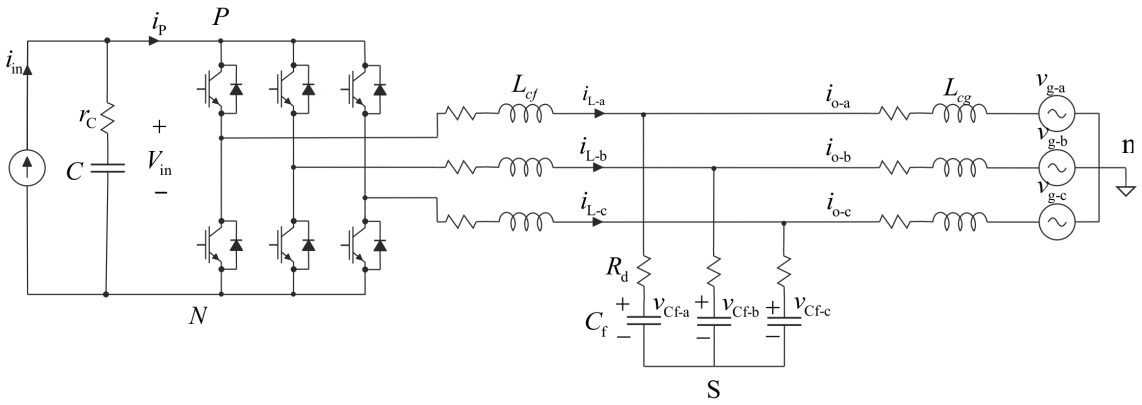

Figure 2.3 *Voltage-sourced inverter connected to grid through an LCL filter.*

for precise control of power factor, power quality, and robust stability. Figure 2.3 shows the grid connection of a current fed voltage-sourced inverter with an LCL output filter.

The dynamics can be divided into large-signal and small-signal behavior. Small-signal behavior describes the operation of inverter around steady-state operating point at which the model is linearized. Linearized state-space allows more simple equations. Appendix A shows the small-signal derivation of the transfer functions for a three-phase voltage-sourced inverter without controllers. The closed-loop modeling is not in the scope of this thesis. In the context of impedance-based interactions, Y_{dd} and Y_{qq} are the most interesting transfer functions, which describe the output admittance d and q-components. The cross-coupled admittances Y_{dq} and Y_{qd} are highly attenuated and thus can be neglected from stability analysis in most cases [36]. Consequently, the output impedance of a three-phase inverter can be solved analytically.

2.2.2 Impedance-based stability criterion

Impedance-based interaction between an inverter and the grid may cause harmonic resonance in grid currents. Harmonic resonance is a widely recognized power quality issue present in most power systems, which results in energy losses, malfunctions in devices, and even system instability. Harmonic current carries no actual power yet it contributes to Joule heating in transmission lines causing additional power losses. On the other hand, the maximum actual power of transmission line decreases as part of the capacity is consumed by oscillating reactive power. In addition, if the

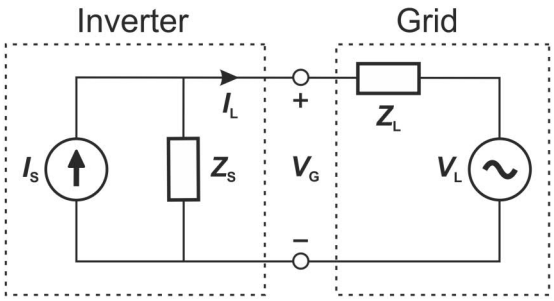

Figure 2.4 *Equivalent source-load system for grid-connected inverter.*

system magnifies this resonating frequency, current increases in every cycle. This eventually leads to instability if the system design or loads do not attenuate the effect.

A grid-connected inverter can be modeled as a Norton equivalent of an inverter connected to a Thevenin equivalent of grid, as shown in Figure 2.4. Inverter acts as a source feeding current to grid, which is represented as a load. Impedance-based stability analysis is carried out by examining the source impedance Z_s and load impedance Z_l.

The current I_L flowing from source to load determines the stability of system. Kirchoff voltage and current laws determine the equation for load current

$$I_L = I_S - I_{Z_S} = (I_S - \frac{V_L}{Z_S}) * (\frac{1}{1 + \frac{Z_L}{Z_S}}) \tag{2.9}$$

The stability analysis of impedance interactions bases on following assumptions

1. inverter is stable when it is not connected to grid
2. grid is stable before connection of inverter
3. impedance models represent real systems and are accurate.

These assumptions make the first term $(I_S - \frac{V_L}{Z_S})$ in (2.9) stable in all cases. Thus, the system stability depends on characteristic polynomial $(1 + Z_L/Z_S)^{-1}$. This polynomial resembles a negative feedback closed-loop transfer function with unity forward gain and Z_L/Z_S feedback gain. Thus, according to linear control theory, the impedance ratio must satisfy Nyquist stability criterion for stable operation [37].

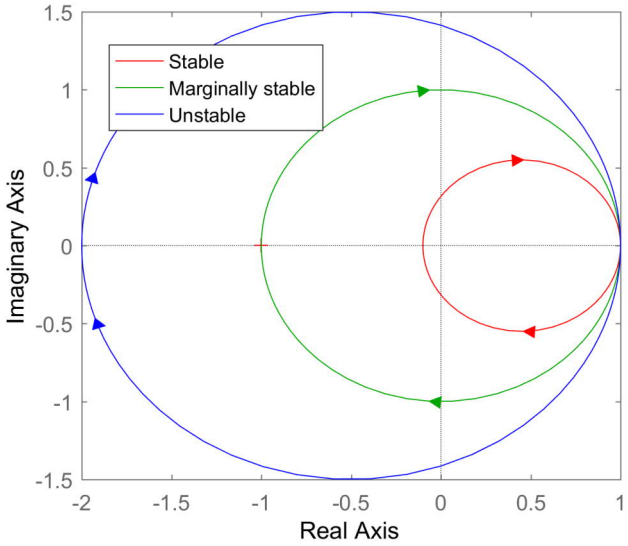

Figure 2.5 *Nyquist curves for unstable (blue), marginally stable (green), and stable (red) systems.*

Nyquist stability criterion states that the stability of the system depends on the location critical point $(-1, 0)$ compared to the locus of polynomial in complex plane. If the locus encircles the critical point in clockwise direction, the system is unstable. On the other hand, a locus passing through the critical point indicates marginal stability, where the system remains in oscillatory state. Figure 2.5 shows Nyquist curves for stable (red), marginally stable (green) and unstable scenarios (blue).

Another approach to stability analysis is examining the gain and the phase of a system in frequency-domain. Bode plots illustrate these characteristics well, and consequently, are widely used for stability examination. According to control theory, the system becomes unstable when the phase is below -180° at the crossover frequency. Applying this to the inverter output impedance and grid impedance yields impedance-based stability criterion. The crossover frequency corresponds to frequency where the impedance magnitudes are equal. Thus, the phase difference has to be less than 180° degrees for system stability. Figure 2.6 presents Bode plots of impedance interaction, based on phase difference at the crossover frequency. Crossover frequency is marked with a black arrow and the corresponding phase difference with a double-headed arrow. Phase difference is approximately 150° and thus the system is stable.

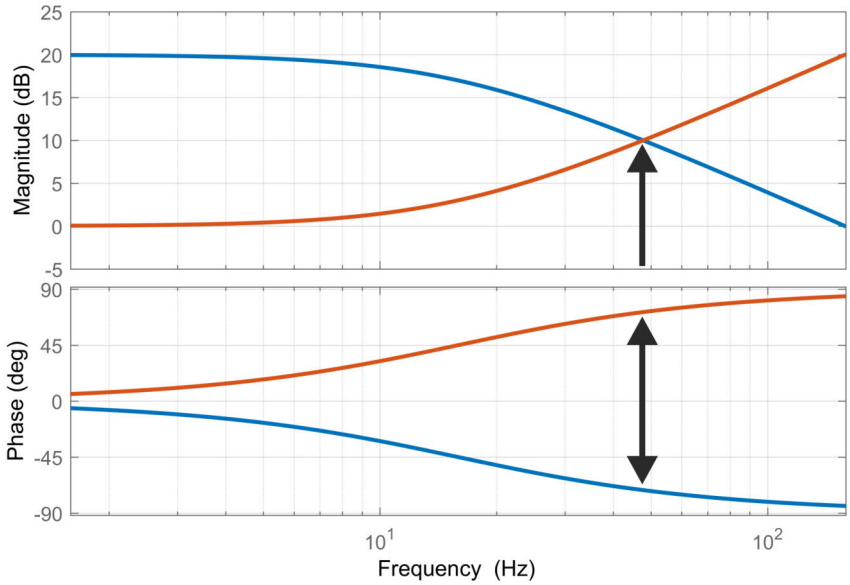

Figure 2.6 *Bode plots of two systems for stability analysis.*

The stability analysis based on the impedance interactions requires information on both output impedance of the inverter and the grid impedance. As briefly shown in Section 3.2.3, the inverter side impedance can be derived with analytic methods. However, the grid impedance is often unknown and currently no unified baselines for modeling a complex grid exist. Thus, deriving methods for modeling and measuring grid impedance are of great importance.

2.2.3 Impact of LCL filter

Most power electronic devices produce high-frequency noise and distortion resulting from the switching effects. Thus, high-frequency filtering is usually required, in order to reach acceptable output waveform. A straight-forward approach to filter current harmonics is to add a series inductor to inverter output. The impedance of an inductor increases linearly with the frequency, which means that higher frequency components encounter larger impedance and are attenuated. However, in high-power applications the required inductance would be high making the solution unnecessarily expensive. In addition, a very large inductance may deteriorate dynamic response of the system. Increasing the order of the filter decreases the required component values. A most common low-pass filter for inverters is a simple

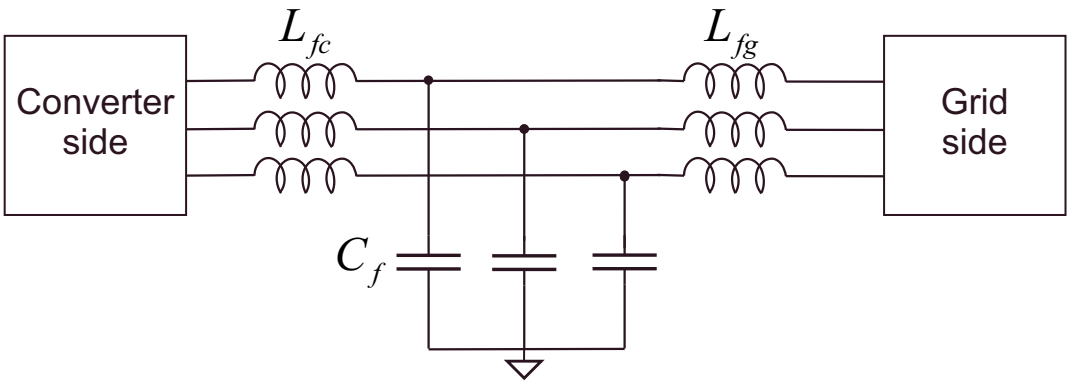

Figure 2.7 *Three-phase LCL-filter for filtering converter output current.*

LCL filter, which consists of two inductors and a parallel capacitor. [38] Figure 2.7 shows a three-phase LCL filter connected between grid and converter.

LCL filter is a third-order filter and due to capacitive and inductive components, it has a resonant frequency ω_{res} given by equation (2.10).

$$\omega_{res} = \sqrt{\frac{L_{fc} + L_{fg}}{L_{fc} L_{fg} C_f}} \tag{2.10}$$

where L_{fc} is converter-side inductance, L_{fg} grid-side inductance and C_f filter capacitance. The transfer function peaks at resonant frequency. The resistances in filter determine the magnitude of the peak. After resonant frequency the gain falls -60 dB/decade providing good attenuation on higher frequencies.

However, an unsuitable LCL filter can have too low attenuation or may even cause additional distortion originating from the resonant behavior. Therefore the filter should be appropriately designed and damped. The grid-connected device may detect the output filter as a part of the grid impedance and it can be considered as source-load system. On the other hand, the grid impedance affects the operation of the filter, as the line inductance is series connected to L_{fg}. Consequently, the resonant frequency of the filter changes. This frequency shift may undermine the designed damping of the filter. The grid inductance may have very different values in different connection locations, which should be taken into account in filter design. According to [20] the resonant frequency of LCL-filter may decrease up to -40% when the grid inductance is increased to 0.1 per-unit (p.u.).

The location of the relay for disconnecting the inverter from grid is usually right after the inverter, before any filters. So, disconnecting an inverter from the grid usually leaves the filter connected to the grid. Therefore, the series-connected LC-branch remains connected to the grid affecting the grid impedance. The LC-part of the filter may introduce additional resonances to the grid impedance.

2.3 Measuring grid impedance

It is imperative to know the frequency-dependent grid impedance for ensuring stability and proper operation of grid-connected converters. The recent dramatic increase in DG induces even larger variance in grid impedance and therefore conventional estimations of grid impedance are not sufficient. Instead, accurate and fast impedance measurements should be achievable for enhanced operation of converters. Online grid impedance measurements can be used for example for fast disconnection of PV inverters from the grid in the case of grid fault [39] or for adaptive control of inverters [5]. This section presents methods for grid impedance measurements suitable for online applications. These can be categorized to passive and active methods.

2.3.1 Passive methods

Passive grid measurement methods utilize only the waveforms already visible in circuit [24], such as harmonic distortions or switching transients. These signals provide the perturbations in current and voltage from which the grid impedance is derived. However, the passive phenomena are often too weak, and the signal-to-noise ratio (SNR) turns out to be too low. In addition, the power spectrum of the distortions in grid may be uneven or unknown. As a result, passive methods are often ineffective when disturbances are weak [40]. Low SNR reduces the accuracy of the measurements and consequently the active methods are widely adopted.

2.3.2 Active methods

In active measurement methods, an excitation signal is injected to grid under measurement. This injection causes perturbation in grid voltage from which the grid impedance is calculated according to Ohm's law in (2.11). If the voltage already

contains harmonics, at least two measurements are required, so that the common-mode harmonic voltage can be removed

$$Z(f) = \frac{U_1(f) - U_2(f)}{I_1(f) - I_2(f)} = \frac{\Delta U(f)}{\Delta I(f)}. \tag{2.11}$$

However, the time in between the measurements should be short enough so that state of grid voltages do not significantly change. The accuracy of the measurements can be increased with the expense of total measurement duration with averaging the results. Repeating measurements multiple times and averaging the results mitigates the measurement noise and errors from fluctuating harmonic content. Performing impedance measurement on multiple frequencies results in grid impedance over wide frequency spectrum. Many different approaches exist for injecting the perturbation current. Most common methods are sine sweep, impulse injection, and use of binary-sequences.

Sine-sweep method perturbs the grid with a sinusoidal single-frequency signal separately for each measured frequency. A sweep over whole spectrum provides the most accurate results with highest achievable SNR. However, as the spectrum is measured one frequency at a time, the duration of the sweep becomes long and therefore sine sweep is unsuitable for fast online estimation. [24] In the experimental section of this thesis, a sine sweep will be used to measure the emulated grid impedance for the best accuracy, as there are no duration requirements for the measurements. An opposite method for long sine-sweep is an impulse injection, where the complete spectrum is measured via a singular impulse. Ideally, an impulse contains very wide range of frequencies and thus Fourier analysis can extract the frequency response on wide spectrum from injected current and voltage responses. The method is very fast, but the energy spectrum of an impulse is unpredictable. In addition, a large impulse may be required especially for strong grids, which may interfere with normal operation of the converters or protection devices.

Applying broadband binary-sequence perturbation provides a good compromise between fast measurement time and good SNR. A commonly used sequence is maximum-length binary sequence (MLBS), which is a periodic and deterministic binary sequence with lowest possible peak factor of energy spectrum. Due to these features, injection can be repeated multiple times for spectral averaging and thus the SNR improves. Consequently, the injection amplitude can be very small compared to other injection types. This minimizes the effect of nonlinear distortions

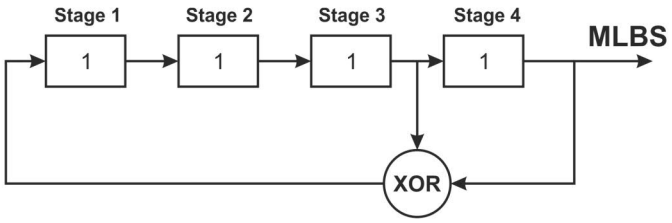

Figure 2.8 *4-bit shift register for MLBS generation.*

and guarantees the normal system operation during the measurement. [24]

In the method using the MLBS, the signal switches between two levels, and the state of the signal can change only at predetermined time steps denoted with Δt. The length of sequence is $N = 2^{n-1}$, where integer n is the number of bits in a sequence. Thus, the duration of one complete periodic sequence is $T = N\Delta t$. In addition, both states occur almost as many times and therefore when levels are mapped to ± 1 the average is very close to zero. Another favorable characteristic is the ease of generation; a simple shift register with XOR feedback generates the signal. Figure 2.8 shows shift register for 4-bit MLBS.

The shift register has a starting value, which can be anything except 0,0,0,0. On every time step Δt, the register values move one step to the right and a new value is created for the first stage. In 4-bit shift register shown above, the new value comes from the XOR function of values at stages 3 and 4. As a result, the complete sequence depends only on the starting values in stages, making the sequence repeat after N time steps. Consequently, the sequence is deterministic and repeatable. Table 2.1 shows the 4-bit MLBS generation starting from preset 1,1,1,1. The period completes after 15 shifts, and shift 16 equals to starting values, thus the sequence starts to repeat.

The periodic and deterministic nature permit the use of averaging techniques for increased SNR. Noise is present in all real-life measurements, and it can cloud the desired results. Repeating measurement multiple times with same pseudo-random sequence yields the same results if the effect of noise is ignored. Therefore averaging over these periods does not affect on measurement result itself, but effectively mitigates noise. The SNR increases by $\sqrt{Q}$ for Q periods of MLBS.

The MLBS generation frequency f_{gen} determines the measurement time and fre-

Table 2.1 *Shift register stages for 4-bit MLBS.*

Shift #	Stage 1	Stage 2	Stage 3	Stage 4
1	1	1	1	1
2	0	1	1	1
3	0	0	1	1
4	0	0	0	1
5	1	0	0	0
6	0	1	0	0
7	0	0	1	0
8	1	0	0	1
9	1	1	0	0
10	0	1	1	0
11	1	0	1	1
12	0	1	0	1
13	1	0	1	0
14	1	1	0	1
15	1	1	1	0
16	1	1	1	1

quency resolution $\frac{f_{gen}}{N}$. As the energy of injection falls, the accuracy of measurement decreases. At $0.45 * f_{gen}$ the energy of the signal has decreased by 3dB, which is often considered as a limit for accuracy. Thus, f_{gen} should be the desired measurement bandwidth divided by 0.45.

2.4 Impedance measurement in dq-domain

The impedance is measured from the voltage response of a known current injection. A typical device for the measurement current injection is a grid-connected inverter, which is typically controlled in synchronous reference frame (SRF). Thus, the desired measurement current is added into inverter output current reference, either in d- or q-component. However, as dq-domain currents and voltages are constants by nature, a sinusoidal component in SRF translates to a complex signal in phase domain. A dq-domain signal equivalent in $\alpha\beta$-domain is

$$\mathbf{x}_{\alpha\beta} = \mathbf{x}_{dq} * e^{j\omega_s t} = (x_d + jx_q)[cos(\omega_s t) - j\sin(\omega_s t)] \tag{2.12a}$$

$$\begin{cases} x_\alpha = x_d \cos(\omega_s t) + x_q \sin(\omega_s t) \\ x_\beta = x_q \cos(\omega_s t) - x_d \sin(\omega_s t) \end{cases} \tag{2.12b}$$

where ω_s is the synchronous frequency of the SRF, which is 50/60 Hz in normal three-phase system. For passive circuits, the d- and q-channel impedances are equal to each other, so measurement on d-channel is sufficient for grid impedance identification. An injection to d-channel with $x_q = 0$ and $x_d = A\sin(\omega_i t)$, where A is the injection amplitude and ω_i frequency, translates to $\alpha\beta$-domain as shown in equation (2.13a).

$$\begin{cases} x_\alpha = A\sin(\omega_i t)\cos(\omega_s t) \\ x_\beta = -A\sin(\omega_i t)\sin(\omega_s t) \end{cases} \tag{2.13a}$$

$$\begin{aligned} \mathbf{x}^{\alpha\beta} &= A\Big[\sin(\omega_i t)\cos(\omega_s t) - j\sin(\omega_i t)\cos(\omega_s t)\Big] \\ &= \frac{1}{2}A\Big\{\Big(\sin(\omega_i t + \omega_s t) + \sin(\omega_i t - \omega_s t)\Big) \\ &\quad -j\Big(\cos(\omega_i t - \omega_s t) - \cos(\omega_i t + \omega_s t)\Big)\Big\} \\ &= \frac{1}{2}A\Big(\sin(\omega_i t + \omega_s t) + j\cos(\omega_i t + \omega_s t)\Big) \\ &\quad +\frac{1}{2}A\Big(\sin(\omega_i t - \omega_s t) - j\cos(\omega_i t - \omega_s t)\Big) \end{aligned} \tag{2.13b}$$

$$\begin{aligned} \mathbf{x}^{\alpha\beta} = &\frac{1}{2}A\Big(-\cos(\omega_i t - \omega_s t + \frac{\pi}{2}) - j\sin(\omega_i t - \omega_s t + \frac{\pi}{2})\Big) \\ &+\frac{1}{2}A\Big(-\cos(\omega_i t + \omega_s t + \frac{\pi}{2}) + j\sin(\omega_i t + \omega_s t + \frac{\pi}{2})\Big) \end{aligned} \tag{2.13c}$$

Equation (2.13c) can be further transformed to exponential form based on Euler's formula

$$\mathbf{x}^{\alpha\beta} = \underbrace{-\frac{A}{2}e^{j(\omega_i t - \omega_s t + \frac{\pi}{2})}}_{positive\ sequence}\underbrace{+\frac{A}{2}e^{-j(\omega_i t + \omega_s t + \frac{\pi}{2})}}_{negative\ sequence}). \tag{2.14}$$

As seen from the equation (2.14), the sinusoidal current injection in d-channel transforms into two different current components in $\alpha\beta$-domain. The components have the same amplitude but they rotate in different direction. In addition, the

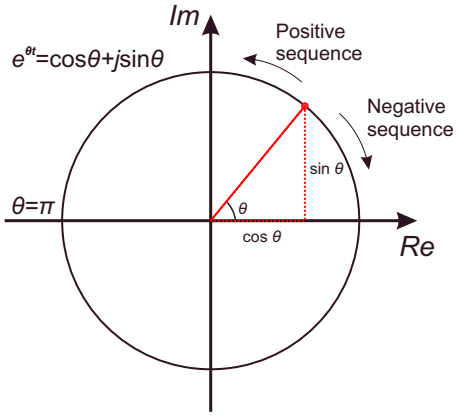

Figure 2.9 *Positive and negative sequences in complex unity circle.*

injection frequency is altered by the synchronous frequency $\omega_s t$ in the transformation from rotating reference frame to stationary reference frame.

In conventional three-phase system analysis, the phasors rotate counterclockwise, which corresponds to $e^{j\omega t}$. However, $\alpha\beta$-domain current injection has a current component with form of $e^{-j\omega t}$ rotating clockwise. Thus, basic analysis tools are not sufficient. The symmetrical component analysis is usually used for unbalanced systems and it bases on linear combination of three different phasor domains; positive, negative, and zero sequences. The positive sequence corresponds to normal counterclockwise rotating system of phasors. On the other hand, negative sequence is similar but rotating in opposite direction [41]. Figure 2.9 illustrates the complex phasors in unity circle and rotation of positive and negative sequences. The current injection appears in both positive sequence and negative sequence, as shown in equation 2.15.

$$\begin{cases} \mathbf{x}_{+}^{\alpha\beta} = -\frac{A}{2} e^{j(\omega_i t - \omega_s t + \frac{\pi}{2})} \\ \mathbf{x}_{-}^{\alpha\beta} = \frac{A}{2} e^{-j(\omega_i t + \omega_s t + \frac{\pi}{2})} \end{cases} \tag{2.15}$$

Consequently, a current injection (measurement) in d-channel at frequency ω_i appears in positive sequency current at $\omega_i - \omega_s$ and in negative sequency current at $\omega_i + \omega_s$. The positive and negative sequence impedances are equal for a passive system [41]. Both of these currents induce a voltage in the corresponding sequence voltage. The dq-transformation of the induced voltages incorporates both voltages in

the resulting voltage d-channel. The measured impedance is given from $Z_d = U_d/I_d$ for each frequency component. However, as presented in equations above, each frequency corresponds to two components in $\alpha\beta$-domain, which are separated by $2*\omega_s$. In conclusion, dq-domain measurement of impedance at frequency ω actually shows the $\alpha\beta$-domain impedances at frequencies $\omega \pm \omega_s$, as shown in equations (2.12a-2.15). This explains the phenomenon where a singular resonant peak appears as two different peaks in dq-domain measurements. Finally, the dq-impedance can be approximated from the phase domain impedances based on conclusions presented in this section. As the d-channel injection appears at phase domain frequencies $\omega_i \pm \omega_s$, the actually measured impedance corresponds to impedance at these frequencies. Thus, an approximated equation for d-channel impedance from phase impedance is given by

$$Z_d(\omega) \approx \frac{Z_{abc}(\omega - \omega_s) + Z_{abc}(\omega + \omega_s)}{2}. \tag{2.16}$$

3. MODELING GRID IMPEDANCE

In this chapter, the characteristics of power grid and grid impedance models are discussed. The methods for grid impedance modeling are derived based on aggregating parts of the system into sub-models. In addition, the time variance and its impact in resonant grids are examined. Lastly, a method for expressing grid impedance analytically from the state-space representation is shown.

3.1 Power grid characteristics

The characteristics of a power grid often define the performance of many grid-connected devices. Especially the performance depends on the sensitivity of the grid parameters to disturbances in grid operation state. This sensitivity defines the strength of the grid. In a strong grid, disturbances resulting from load changes or harmonic currents have only a minor effect on grid. On the other hand, a weak grid suffers from voltage changes during power consumption transients - for example, the inrush current of an induction machine may cause severe fall in voltage and consequently flicker issues. In addition, harmonic currents distort the voltage more in weaker grids.

3.1.1 Grid topology

The main factors defining the strength of the grid are location, topology, consumption type, and type of grid elements. Topology of a power grid describes the shape and complexity of the grid. Typically, the grid can be classified to one of the following categories: radial, looped, or mesh, based on increasing complexity. A radial grid is the simplest configuration, which consists of radial lines diverging from power supply to consumption. Radial topology is common in rural regions with low power levels, long transmission lines, and few consumers. A looped topology is similar to radial grid, but in addition has parallel lines connecting multiple radial lines into

a larger system. Thus, different parts of the system networks can balance each other and disconnection of a singular line does not necessarily result in blackout of a consumer group as the parallel lines can supply the power. Lastly, the most complex grid topology, mesh, is mainly found in cities and other high power demand areas with dense consumer base. A meshed grid comprises of several interconnected power lines, possibly with no easily identified main power lines. Hence, the power flow analysis in a mesh grid is very complicated and often impossible. Due to high amount of parallel lines and alternative paths for power flow, the mesh is typically a strong grid topology in which voltage level is stiff. In addition, a fault in singular line usually affects only a small area as multiple other paths for power are available.

3.1.2 Power quality standards

The modern society relies on access to reliable electric power. Thus, adequate power quality of this electricity supply is essential. Insufficient power quality may cause issues of wide scale, ranging from a minor inconvenience up to a fire hazard or expensive device breakdown. Typical significant issues include for example equipment damage, supply interruptions, excess flickering, malfunctioning of devices, and decreased efficiency. The regulations and standards aim to mitigate these issues and ensure well-functioning power system.

The quality of power is a product of multiple parameters, most of which are applied to voltages in the three-phase AC system. A phase voltage should have certain amplitude and frequency, and sinusoidal form. In addition, all three phases should have balanced voltages. One of the most visible issue to consumers are interruptions of power supply, which may escalate to a major blackout in extreme cases.

European Standard EN-50160 sets limitations for several voltage characteristics, and provides the base for Finnish power standard SFS-EN 50160. According to EN-50160, voltage frequency should remain 99.5 % of time in 50 Hz$\pm$1% and all the time between 47 and 52 Hz. The amplitude of voltage is limited to $U_n\pm$10% for 95% of the time, although in SFS-EN 50160 the lower limit is set to -15 %. [42]

One of the most important regulation concerning grid-connected inverters is the limit on harmonic voltages. Non-linear components of power grid may draw or inject current, which is not necessarily sinusoidal, but instead distorted. The impedances in system transfer these distorted currents into distorted voltages. When sinusoidal

Table 3.1 *Harmonic voltage limitations according to EN-50160 -standard. [42]*

Order of harmonic	Relative voltage (%)
3	5.0
5	6.0
7	5.0
9	1.5
11	3.5
13	3.0
15	0.5
17	2.0
19	1.5
21	0.5
23	1.5
25	1.5

signal distorts, Fourier analysis can deconstruct the non-sinusoidal signal to multiple sinusoids. Harmonic signals are sinusoids at fundamental frequency multiplied with an integer. For example, third order harmonic voltage has frequency of 150 Hz in 50 Hz grid. EN 50160 sets regulations to maximum harmonic voltage levels, which are compared to level of fundamental frequency voltage, as shown in table 3.1.

In addition, an important criterion is total harmonic distortion (THD) which accounts for all harmonic frequencies. THD is the ratio of sum of all harmonic powers to the power of fundamental frequency, given from

$$\text{THD} = \frac{\sqrt{\sum_{m=1}^{40} V_m^2}}{V} \tag{3.1}$$

where V_m is the n order harmonic voltage and V is the fundamental frequency voltage. THD is often used as an indicator of power quality of load or supply. The highly distorted voltage in Figure 2.1 in Section 2.1.2 has THD value of 20.7 % based on equation (3.1).

3.1.3 Transformer impedance

A transformer consists of two inductor coils coupled with a common magnetic core. Current in the primary side winding generates a changing magnetic field, which in turn induces a voltage in the secondary winding. The voltage ratio over the transformer is proportional to ratio of turns in the windings. Thus, transformers are used to modify the voltage levels in different parts of the grid. Voltage levels in transmission are typically high, up to 400 kV of main transmission grids, in order to mitigate ohmic losses of conductors. On the other hand, distribution voltage is usually only 400 V or 207 V. Hence, transformers are very common elements in all AC power systems. [43]

Transformer affects the grid impedance through two mechanisms: it changes the impedance seen through the transformer and adds an additional series impedance. In order to consider different voltage levels, the impedance must change accordingly. Base values are a commonly used tool for different voltage levels, for which the base voltage and base power are defined. These define the base value for impedance $Z_B = U_B^2/S_B$. For a transformer, the power is equal on both sides and thus Z_B changes proportional to ratio of squared voltages when moving through transformer. Consequently, analysis can neglect the change in voltage level if the impedances at the other side of transformer are reduced corresponding to base values. [44] Hence, reflecting the grid impedance from primary to secondary side is given by

$$Z_1' = \left(\frac{U_2}{U_1}\right)^2 * Z_1 \tag{3.2}$$

Figure 3.1 shows equivalent circuit for a transformer, where subscript P denotes primary side and S secondary side. X_M is the magnetizing reactance and R_C the iron losses in the transformer core. The current through parallel branch is small, and thus the impedance model is sufficiently accurate when neglecting the parallel branch. After this assumption, primary and secondary sides can be combined and the impedance model of the transformer is reduced to series inductance and resistance. [44]

Usually transformer's plate values include relative inductance x_k and relative resistance r_k, which are usually $6 \ldots 15$ % and $1 \ldots 2$ %, respectively [44]. The values are percentages of base impedance on the chosen side of transformer, so the actual

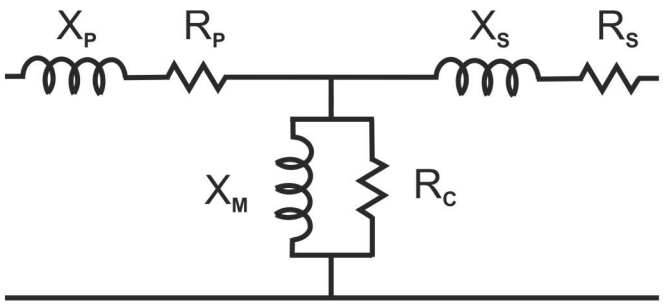

Figure 3.1 *Equivalent circuit for transformer.*

values are given by $R_k = r_k * Z_B$ and $X_k = x_k * Z_B$.

3.1.4 Resonant circuits

Inductances and capacitances of power grid cause the imaginary part of impedance, reactance. Pure inductance has impedance of $Z\angle 90°$ and capacitance $Z\angle -90°$, resulting in a phase shift of 180°. Thus, with equal magnitudes the series connected impedances counteract each other. The impedances of capacitor and inductor are given by $Z_C = (j\omega C)^{-1}$ and $Z_L = j\omega L$, where ω is the angular frequency, C the capacitance, and L the inductance. The capacitive impedance is inversely proportional to frequency and the inductive impedance is linearly dependent on the frequency. Thus, at a certain frequency, capacitive and inductive reactances will have equal magnitudes. This frequency is the resonant frequency, at which the series or parallel resonance occurs. Equation 3.3 determines the resonant frequency

$$f_{res} = \frac{1}{2\pi\sqrt{LC}}. \tag{3.3}$$

In series resonance, the impedance of ideal LC-circuit approaches zero at the resonance frequency. On the other hand, ideal parallel-resonant circuit has impedance approaching infinity near resonance frequency. Figure 3.2 presents the parallel and series resonant RLC-circuits.

The resistance R damps the resonance phenomenon, and thus attenuates the peaking of the impedance. Figure 3.3 shows the frequency dependent impedance for resonance circuits shown in Figure 3.2, when $C = 10^{-4}$ F and $L = 10^{-3}$ H, so the resonance frequency is $f_{res} = 503$ Hz. In addition, a damping resistor has been added

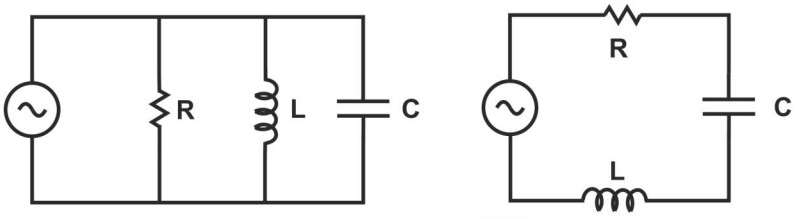

Figure 3.2 *Parallel (left) and series (right) resonant RLC-circuits.*

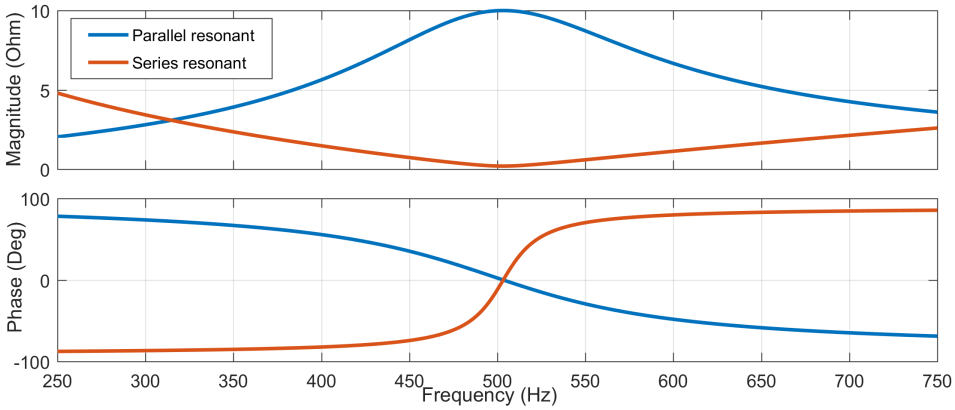

Figure 3.3 *Impedance of parallel (blue) and series (red) resonant circuits shown in figure 3.2.*

for better readability, 10 Ω and 0.2 Ω for parallel and series circuits, respectively.

As most power systems contain both inductances and capacitances, both series and parallel resonances occur frequently. Especially parallel resonances may have drastic impact on grid impedance in the form of peaking of grid impedance, as shown in Figure 3.3. Transmission lines and transformers are typically inductive, and household loads contain multiple sources of capacitance, which together may form parallel resonant circuit. The power system typically involves large amount of resistive loads, which mitigate the impact of the resonance. However, significant share of resistive consumer loads may disconnect during nighttime, thus decreasing resonance mitigation.

3.1.5 Short-circuit ratio

An important characteristic for a power grid is the short-circuit power level which depicts the power in certain point of grid at a three-phase fault. Comparison of this short-circuit power to the nominal power of the system is defined as the short-circuit ratio (SCR), which is given by

$$\mathrm{SCR} = \frac{S_{sc}}{S_n} \tag{3.4}$$

where S_{sc} is the short circuit power and S_n is the nominal power [17]. The short circuit power can be further calculated from

$$S_{sc} = \frac{U_g^2}{Z_g} \tag{3.5}$$

where U_g is grid voltage and Z_g grid impedance. Therefore, SCR value is inversely proportional to grid impedance. The value of SCR defines the grid strength; larger ratios indicate stronger grid.

Often the stiffness of a grid is defined using SCR ratio. Unambiguous reference values are not present in literature, but often a power grid with SCR above 20-25 is considered strong and SCR below 2.5 to 10 a weak grid [17, 45–47]. DG connected to remote rural locations may encounter extremely low SCR values, especially when the production capacity is high. Some publications have considered as low as 1.2 SCR values for grid-connected devices [45, 48]. However, SCR value of 10 is often used as a design parameter for grid-connected inverters [13, 20, 49]. The SCR value of 10 corresponds to 10% per-unit grid impedance.

3.1.6 X/R ratio

The ratio of grid reactance X to grid resistance R is a commonly used indicator for characterizing a transmission line. This ratio does not define the strength of the grid as it examines only a ratio instead of absolute values, but regardless it provides valuable information of the grid impedance. The grid impedance is analyzed in complex plane with the reactive component as imaginary value and it can be evaluated from

$$Z_g = R + jX. \tag{3.6}$$

Equation (3.7) defines the angle of the impedance

$$Z_g = \tan(\frac{X}{R}). \tag{3.7}$$

Based on these equations, grid impedance magnitude and phase define the passive grid reactance and resistance.

Typically, HV transmission lines designed for high power levels have very high X/R values, as use of large diameter conductors minimize the resistance of line. Therefore, neglecting the resistive part of impedance may not lead to significant error, so this assumption can be made for very high X/R lines. On the other hand, DG is often connected to a remote location grid connection and the transmission line is long. Thus, weak interconnection with rest of the power grid typically means higher resistance of transmission line, which means lower X/R-ratio. Based on these characteristics, X/R ratio is occasionally used for recognizing a weak grid [50].

3.1.7 Definition of weak grid

The definition of weak grid varies in literature, but in most cases weak grid refers to low SCR value. However, determining SCR values for weak grid are incoherent ranging from 2.5 to 10, because different applications and scenarios consider grid strength differently. Also low X/R-ratio (for example below 0.5) is sometimes used as an indicator for weak grid [50]. Low X/R-ratio translates to relatively high resistance of grid, which is typical for LV lines with small conductor diameter. In context of grid-connected power electronics, a weak grid is often described simply with a large grid inductance value [3,12,16,19,23]. These approaches are partially in conflict with each other, and thus uniform definition cannot be derived. Connection of power electronics to weak grid is of special interest, as the grid weakness imposes new challenges for stable operation.

In large DG systems or high-voltage DC (HVDC) links the nominal powers may have very large values in comparison with short-circuit power. Thus, the SCR values for such systems are decreased even further. These conditions are commonly recognized as ultra weak grids, where the SCR values range from 1 to 2.5 [14,51,52]. Consequently, new limitations are set to system, e.g. maximum power output of multiple parallel-connected inverters might face limitations. Ultra weak grids impose very challenging operation conditions for voltage-sourced converters (VSC).

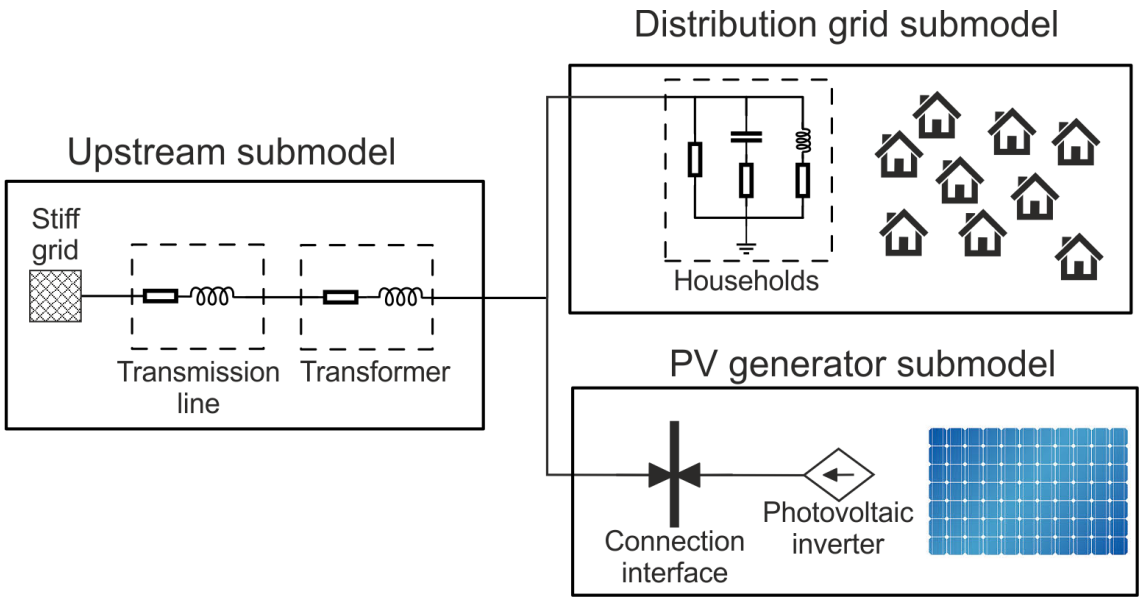

Figure 3.4 *Grid impedance analysis based on submodels.*

3.2 Composition of grid impedance

The power system consists of large number of transmission lines, other grid elements, generation, and loads. In context of grid impedance, these elements appear as series- and parallel-connected impedances. The impedance topology depends on the location of point of connection (PoC), and thus the PoC sets the inspection frame for grid impedance. The system can be effectively separated to subsystems based on type and location of impedances, compared to the PoC. This sub-modeling simplifies the analysis as some of the impedances are grouped together. Subsystems used in this thesis are upstream grid, local distribution grid, and DG, all of which can be modeled as entities relatively easy. Figure 3.4 presents the approach based on sub-models and aggregation of impedance elements of similar type and location.

3.2.1 Upstream grid

The foundation of a power system is the HV power grid, which usually is nationwide. Virtually all local systems are connected to this HV main grid, and thus the entire power grid is interconnected. The power grid can be categorized into layers based on voltage and power levels, so that the highest layer is the main grid, which has the voltage of 110 or 400 kV in Finland. On the other hand, a normal household

customer locates to the lowest layer at LV distribution grid. Traditionally, the power flow direction has been from higher to lower level, but the increasing amount of DG may in some cases feed the power to higher voltage levels. The connection towards the main grid is defined as the *upstream grid*.

In this thesis, upstream grid refers to sub-grid consisting of transmission from PoC to the HV main grid. The HV grid is approximated to be very strong (SCR of 200) and thus have negligible impedance compared to rest of the upstream grid [50]. Transmission elements of upstream grid are modeled in the guidelines of traditional power system analysis [44]. The medium-voltage (MV) overhead transmission lines are depicted as series inductance and reactance, as the capacitance becomes significant only in HV lines or underground cables. The cables have significant capacitance and neglecting resulting resonances would lead to inaccurate result. Therefore, π-model is used for modeling transmission cables. Transformers are modeled as series inductance and resistance, based on typical per-unit values, as explained in Section 3.1.3. Upstream grid is usually essentially inductive with varying amount of series resistance.

3.2.2 Local distribution system

A local distribution grid consists mainly of regular households, which contain very large number of small-scale loads. The exact modeling of all the singular loads is time-consuming and complex. In addition, precise load characterization for households is difficult, due to very large variance of load types. However, cluster of households can be approximated with a simplified model with only a few equivalent impedances. The general assumptions for creating a clustered sub-model are

- households locate relatively close to each other, i.e. transmission distances are negligible
- all households within cluster are relatively similar
- resistive loads consume the bulk of the household power consumption
- inductive and capacitive loads are significantly smaller than resistive loads.

From the impedance point of view, all the household loads are connected in parallel. Therefore, combining loads of similar type becomes trivial. All the resistive loads

can be substituted by an equivalent resistor, size of which can be approximated with $R = V^2/P$, where V is the line-to-line voltage and P the power consumption of the household cluster. The same procedure applies to loads which are assumed to be purely either inductive or capacitive. A significant difference origins from the different parallel behavior of capacitors and inductors. Parallel connecting resistors or inductors effectively decreases the equivalent impedance. However, equivalent capacitor for multiple parallel-connected is the sum of the capacitances $C_{eq} = \sum C$. Thus, the household cluster capacitance increases to a significant value, due to sheer amount of parallel-connected small capacitances. According to [53], the equivalent capacitance for a typical household varies in the range of $0.5 \ldots 6$ μF.

With many households close to each other, the equivalent capacitance may rise to hundreds of μF. As stated in Section 3.2.1, the upstream grid is usually mainly inductive. Consequently, capacitive distribution grid may form a resonant circuit with mainly inductive upstream grid, which can have dramatic effect on grid impedance at certain frequencies. Another distinctive phenomenon in distribution systems is a strong time variance, which may significantly affect the grid impedance. This is discussed further in Section 3.3.

3.2.3 DG system and parallel inverters

When the volume of distributed generation (DG) increases, the impact on power system becomes more apparent. DG can locate within distribution network as small-scale units, as independent large-scale farms, or anything from between of these options. Hence, type of DG subsystem relies on configuration of DG itself. As stated previously, virtually all DG is connected to power grid via a converter, and thus the converters and filters form the grid impedance. Section 2.2.3 described the impact of LCL filter, and this section discusses the converter impedance as seen from the grid.

A grid-connected converter interacts with the grid through its output impedance, and thus the grid impedance is affected by the output impedance of the converter. However, a grid-connected converter is an active element, unlike passive elements of transmission system or loads. This means that the control of the converter affects the output impedance making the output impedance very complex to model. When the behavior of the converter itself is in focus, the output impedance is derived from the dynamic behavior. In this thesis, a simplified inverter model suffices, as

the aim is to approximate the impact of output impedance on the grid impedance. The model includes only the inner current control loop, so possible feedforwards, control delays, grid synchronizations, and other control systems are not taken into consideration. This results in a minor error, however, in the scope of this thesis this simplification is justified.

Output current control of an inverter makes the output impedance appear capacitive within the control bandwidth, which means higher impedance in frequencies below bandwidth. On the other hand, inductive output filter incorporates inductance to the output impedance. The inductance has significant effect on high frequencies. Between these regions the output impedance appears resistive. Thus, a series RLC-branch approximates the output impedance of an inverter reasonably well. [34]

The inverter dynamics are usually analyzed in dq-domain. In dq-domain, the output impedance is a 2x2-matrix

$$\underbrace{\begin{bmatrix} u_d \\ u_q \end{bmatrix}}_{\mathbf{U}} = \underbrace{\begin{bmatrix} Z_{dd}(s) & Z_{dq}(s) \\ Z_{qd}(s) & Z_{qq}(s) \end{bmatrix}}_{\mathbf{Z}} \underbrace{\begin{bmatrix} i_d \\ i_q \end{bmatrix}}_{\mathbf{I}} \tag{3.8}$$

where $Z_{dq}(s)$ and $Z_{qd}(s)$ are cross-coupled impedances. According to [34], equivalent impedance parameters for output impedance of an inverter can be derived in dq-domain. The cross-coupled impedances are small, and are assumed negligible. The equivalent impedance for d-component can be calculated from

$$Z_{eq-dd} = L_{eq}s + \frac{1}{C_{eq}s} + R_{eq} = L_{fc}s + \frac{1}{(L\omega_s^2 + K_{CC}V_{in})^{-1}s} + \frac{K_{CC}V_{in}}{\omega_{z-CC}} \tag{3.9}$$

where L_{fc} is converter output filter inductance, ω_s is fundamental angular frequency, K_{CC} is the current controller gain, V_{in} is input voltage, and ω_{z-CC} is angular frequency of the current controller zero. On the other hand, the q-component of the impedance consists of a series RLC-circuit is equal to d-component, but in addition, the grid synchronization method adds an additional parallel impedance component. This component behaves as a negative resistor, which is impossible to model using passive components. However, negative resistance behavior appears only within the grid synchronization control bandwidth, which is usually only a few tens of Hz. Thus, the impact of negative resistor is limited and this component is removed from impedance equation. Consequently, it is assumed that $Z_{qq}(s) = Z_{dd}(s)$. [34]

The output impedance is now approximated in dq-domain. However, the models are constructed as single phase equivalent circuits, so the inverter impedance should be transformed to phase domain. Inverse Park's matrix produces sinusoidal signals and thus cannot be used, because the impedance is the ratio of sinusoidal current and voltage, not a sinusoid itself. According to [54], equation (3.10) transforms dq-admittance to phase domain

$$Y_{abc} = \frac{1}{2}\Big[Y_{dd}(s) + Y_{qq}(s) + j\Big(Y_{qd}(s) + Y_{dq}(s)\Big)\Big] \tag{3.10}$$

when $s = j(\omega - \omega_s)$ and admittances are similar to impedance components in equation (3.8). In this analysis, the cross-coupled components are neglected. In addition, because the effect of grid synchronization to impedance q-component was approximated to be small, impedance d and q-components are equal. Therefore, phase impedance equation (3.11) can be derived from equation (3.10).

$$Z_{abc} = \frac{1}{2}\Big[Z_{dd}\Big(j(\omega - \omega_s)\Big) + Z_{qq}\Big(j(\omega - \omega_s)\Big)\Big] = Z_{dd}\Big(j(\omega - \omega_s)\Big) \tag{3.11}$$

Combining equations (3.9) and (3.11) results in a depiction of inverter output impedance in phase domain

$$Z_{inv-abc} = L_{eq}j\omega - L_{eq}j\omega_s + \frac{1}{C_{eq}j\omega - C_{eq}j\omega_s} + R_{eq} \tag{3.12}$$

where fundamental frequency component produces constant imaginary terms $-L_{eq}j\omega_s$ and $-C_{eq}j\omega_s$. These constant terms are problematic, as they cannot be depicted using passive elements. Figure 3.5 shows the output impedance of an inverter with $L_{eq} = 5$ mH, $R_{eq} = 28\ \Omega$, and $C_{eq} = 7.3\ \mu$F calculated using equation (3.12) and approximated equation where constant terms are assumed to be zero. The approximated impedance matches the equation (3.12) well, especially in higher frequencies. The output impedance of the inverter has the greatest impact on grid impedance when the output impedance magnitude is low. Figure 3.5 shows that approximation produces significant error only in very low frequencies. In addition, ignoring negative resistance from grid synchronization causes error only to very low frequencies. However, at low frequencies the impedance magnitude is very large, and thus this error diminishes. Therefore, approximation is adequate and using it is justified. In

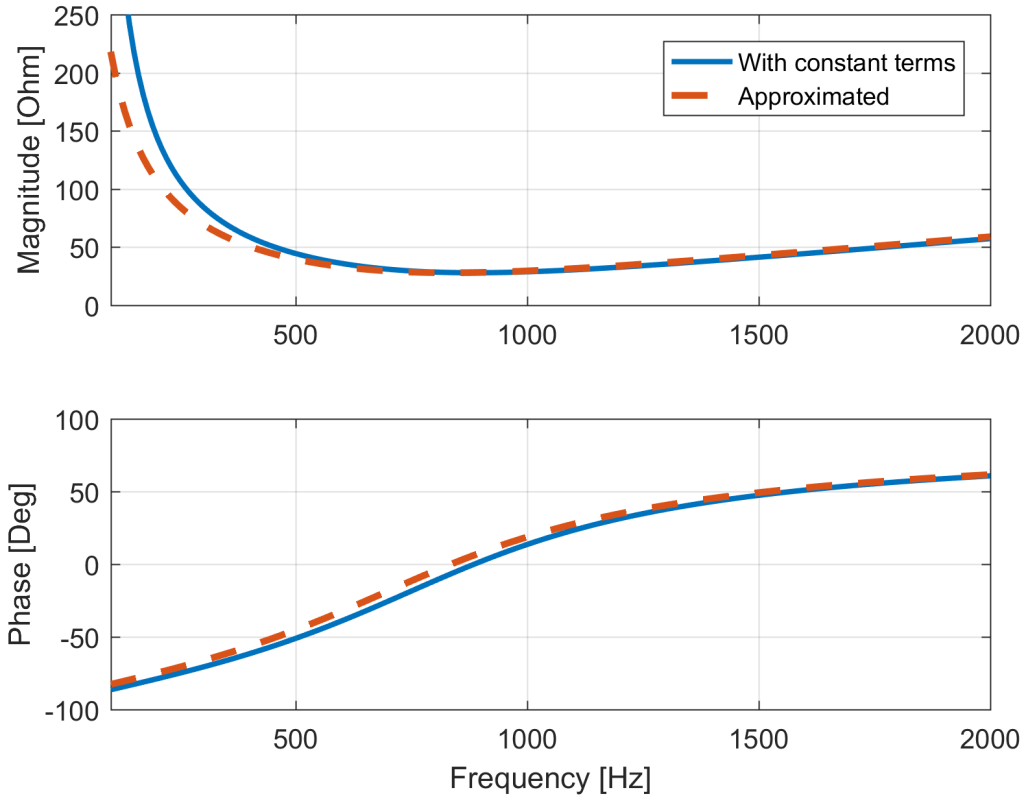

Figure 3.5 *Inverter impedance in phase domain with (blue) and without (orange) constant terms.*

this thesis, approximated equation (3.13) is used for output impedance of inverters.

$$Z_{inv-o} = L_{eq}j\omega + \frac{1}{C_{eq}j\omega} + R_{eq} \tag{3.13}$$

3.3 Time variance in grid impedance

The impedance of static grid elements remain almost constant over time. However, the switching status of the grid and load impedances may encounter even drastic changes depending on time of the day. This time variance should be taken into account when considering grid impedance values. In some cases, the variance may shift the grid impedances phase angle up to 90 degrees or double the magnitude. Design of grid-connected device should consider these possibilities.

The switching status of the grid makes usually only minor changes to grid impedance, unless topology-changing changes are made. However, a change in switching status generates quickly fading transient in current and voltage, which may disturb ongoing impedance measurement. The state of tap changers in transformers or static VAR compensators affect the grid inductance or capacitance. Especially capacitor banks may contribute to resonances, which affect on impedance at certain frequency. In addition to normal operation of system, faults in power grid may have dramatic and unexpected impact on grid impedance. Circuit breakers and other grid devices are designed to remove the faulty sub-grid or transmission line from the grid to minimize the effect of excessive fault currents. The area directly affected usually experiences a blackout, but surrounding areas might instead see an increase in grid impedance, as the grid weakens when faulty parallel lines are removed.

Changes in loading status of the grid are a major cause of daily time variance in the grid impedance. In LV distribution grid the changes have two main causes; customer loads and unpredictability of small-scale generation. As the penetration of small-scale renewable energy sources increases, the variance in DG increases. Especially PV systems encounter abrupt changes in production, and on the other hand show strong time-dependent behavior correlating to time of the day. Thus, the impedance of DG is in constant change. In addition, the consumption pattern of customers has a great impact on the grid impedance. Turning on an appliance effectively means addition of a parallel impedance to the power grid.

In [55] the grid impedance from a public LV distribution grid of 49 households was measured. The results showed dramatic time variance in grid impedance, and especially resonances were clearly present. At 1.8 kHz the impedance has daytime magnitude of 0.5 Ω, which is increased to 1.3 Ω during nights (between 22:30-05:30) due to parallel LC-resonance. Thus, the grid impedance encountered large time variance with a daily repeating pattern. The changes in grid impedance were attributed mostly to capacitive loads and large amount of DG. [55]

Figure 3.6 demonstrates the time-dependent grid impedance for a simple LC-resonant system. The system corresponds to sub-model system in Figure 3.4 shown in Section 3.2 with no distributed generation. The system consists of inductive upstream grid and capacitive distribution grid, where the active power consumption strongly correlates to time of the day. This appears as strong variance in the magnitude of resonant peak appearing at 300 Hz. Other variables, such as equivalent capacitance

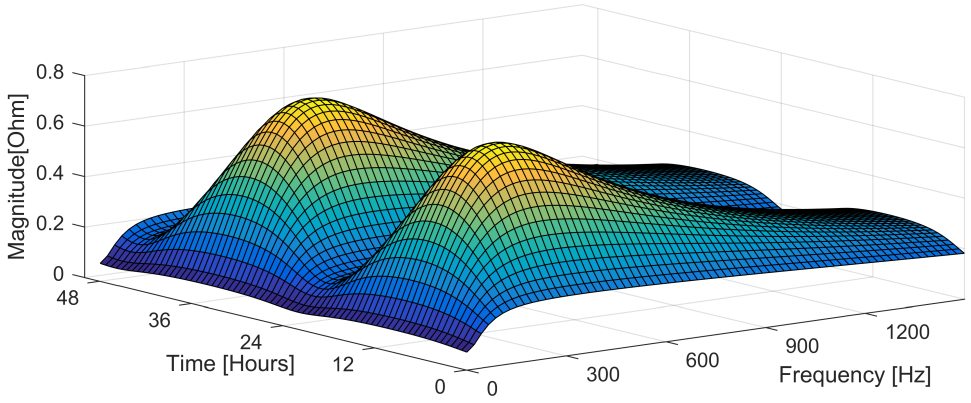

Figure 3.6 *Magnitude of time-variant grid impedance from a resonant grid.*

of the system, were considered constant, which simplifies the analysis. However, it is apparent that time-dependency of the grid impedance may alter the operation conditions even drastically, and thus modeling based on constant variables may result in inaccuracies. In order to avoid possible instability, time-dependent models or online measurements of grid impedance are strongly suggested.

3.4 State-space representation of grid impedance

A state-space representation is widely used in control engineering to model a dynamic system as differential equations of input, output, and state variables. Equation (3.14) presents the generalized first order state space of a linear system

$$\begin{cases} \dot{\mathbf{x}} = \mathbf{A}\mathbf{x} + \mathbf{B}\mathbf{u} \\ \mathbf{y} = \mathbf{C}\mathbf{x} + \mathbf{D}\mathbf{u} \end{cases} \tag{3.14}$$

where $\mathbf{x}$ is state vector, $\dot{\mathbf{x}}$ is derivative of state vector, $\mathbf{u}$ is input vector, $\mathbf{y}$ is output vector, and $\mathbf{A}$-$\mathbf{D}$ are state matrices. As the inductors voltage and capacitor current equations are differential equations, a state space is suitable approach. The grid impedance can be seen as a load effect for the inverter output. Figure 3.7 shows the connection of current source (inverter) to a certain grid, which can be represented by state spaces. The input, output and state vectors are

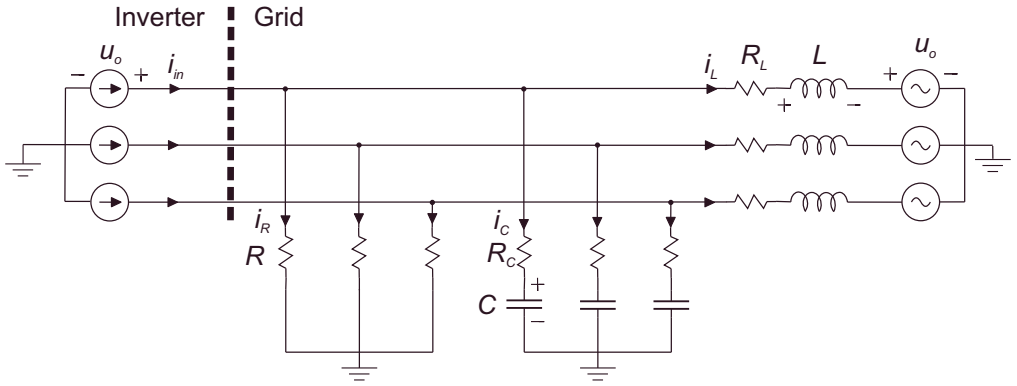

Figure 3.7 *Inverter-grid connection for state space impedance analysis.*

$$\mathbf{u} = \begin{bmatrix} i_{in} \\ u_o \end{bmatrix} \qquad \mathbf{y} = \begin{bmatrix} u_{in} \\ i_o \end{bmatrix} \qquad \mathbf{x} = \begin{bmatrix} i_L \\ u_C \end{bmatrix}. \tag{3.15}$$

The base equations are

$$u_L = u_{in} - r_L i_L - u_o \tag{3.16a}$$

$$i_C = i_{in} - i_R - i_L \tag{3.16b}$$

$$u_{in} = R_C i_C + u_C \tag{3.16c}$$

Substituting (3.16b) into (3.16c) gives

$$u_{in} = R_C(i_{in} - i_R - i_L) + u_C \tag{3.17}$$

from which the input voltage can be solved using $i_R = u_{in}/R$

$$u_{in} = \frac{R_C}{1 + \frac{R_C}{R}} i_{in} - \frac{R_C}{1 + \frac{R_C}{R}} i_L + \frac{1}{1 + \frac{R_C}{R}} u_C. \tag{3.18}$$

Substituting equation (3.18) to (3.16b) gives the equation for capacitor current

$$i_C = \Big(1 - \frac{R_C}{R(1 + \frac{R_C}{R})}\Big) i_{in} + \Big(\frac{R_C}{R(1 + \frac{R_C}{R})} - 1\Big) i_L - \frac{1}{R(1 + \frac{R_C}{R})} u_C. \tag{3.19}$$

The state variables derivatives base on equations for capacitor current $i_C = C\frac{\mathrm{d}u_C}{\mathrm{dt}}$ and inductor voltage $u_L = L\frac{\mathrm{d}i_L}{\mathrm{dt}}$, and thus the state variable derivatives are solved

using equations (3.18, 3.19, 3.16a), and (3.16b)

$$\frac{\mathrm{d}i_L}{\mathrm{dt}} = \frac{AR_C}{L}i_{in} - \frac{AR_C + R_L}{L}i_L + \frac{A}{L}u_C - \frac{1}{L}u_o \tag{3.20}$$

$$\frac{\mathrm{d}u_C}{\mathrm{dt}} = \Big(\frac{1}{C} - \frac{AR_C}{RC}\Big)i_{in} + \Big(\frac{AR_C}{RC} - \frac{1}{C}\Big)i_L - \frac{A}{RC}u_C, \tag{3.21}$$

where $A = \frac{R}{R+R_C}$. The equations are transformed to dq-domain, which introduces cross-coupling terms to equations

$$\frac{\mathrm{d}i_{Ld}}{\mathrm{dt}} = \frac{AR_C}{L}i_{ind} - \frac{AR_C + R_L}{L}i_{Ld} + \omega_s i_{Lq} + \frac{A}{L}u_{Cd} - \frac{1}{L}u_{od} \tag{3.22a}$$

$$\frac{\mathrm{d}i_{Lq}}{\mathrm{dt}} = \frac{AR_C}{L}i_{inq} - \frac{AR_C + R_L}{L}i_{Lq} - \omega_s i_{Ld} + \frac{A}{L}u_{Cq} - \frac{1}{L}u_{oq} \tag{3.22b}$$

$$\frac{\mathrm{d}u_{Cd}}{\mathrm{dt}} = \Big(\frac{1}{C} - \frac{AR_C}{RC}\Big)i_{ind} + \Big(\frac{AR_C}{RC} - \frac{1}{C}\Big)i_{Ld} - \frac{A}{RC}u_{Cd} + \omega_s u_{oq} \tag{3.22c}$$

$$\frac{\mathrm{d}u_{Cq}}{\mathrm{dt}} = \Big(\frac{1}{C} - \frac{AR_C}{RC}\Big)i_{inq} + \Big(\frac{AR_C}{RC} - \frac{1}{C}\Big)i_{Lq} - \frac{A}{RC}u_{Cq} - \omega_s u_{od} \tag{3.22d}$$

where ω_S is the synchronous frequency of the dq-frame. The equations in (3.22) correspond to state space presentation shown in (3.14). Thus, the system can be represented in matrix form

$$\dot{\mathbf{x}} = \underbrace{\begin{bmatrix} -\frac{(AR_C+R_L)}{L} & \omega_s & \frac{A}{L} & 0 \\ -\omega_s & -\frac{(AR_C+R_L)}{L} & 0 & \frac{A}{L} \\ (\frac{AR_C}{RC} - \frac{1}{C}) & 0 & -\frac{A}{RC} & \omega_s \\ 0 & (\frac{AR_C}{RC} - \frac{1}{C}) & -\omega_s & -\frac{A}{RC} \end{bmatrix}}_{\mathbf{A}} \mathbf{x} + \underbrace{\begin{bmatrix} \frac{AR_C}{L} & 0 & -\frac{1}{L} & 0 \\ 0 & \frac{AR_C}{L} & 0 & -\frac{1}{L} \\ (\frac{1}{C} - \frac{AR_C}{RC}) & 0 & 0 & 0 \\ 0 & (\frac{1}{C} - \frac{AR_C}{RC}) & 0 & 0 \end{bmatrix}}_{\mathbf{B}} \mathbf{u} \tag{3.23}$$

$$\mathbf{y} = \underbrace{\begin{bmatrix} -AR_C & 0 & A & 0 \\ 0 & -AR_C & 0 & A \\ 1 & 0 & 0 & 0 \\ 0 & 1 & 0 & 0 \end{bmatrix}}_{\mathbf{C}} \mathbf{x} + \underbrace{\begin{bmatrix} AR_C & 0 & 0 & 0 \\ 0 & AR_C & 0 & 0 \\ 0 & 0 & 0 & 0 \\ 0 & 0 & 0 & 0 \end{bmatrix}}_{\mathbf{D}} \mathbf{u} \tag{3.24}$$

where the dq-domain input, output, and state vectors are

$$\mathbf{u} = \begin{bmatrix} i_{ind} \\ i_{inq} \\ u_{od} \\ u_{oq} \end{bmatrix} \qquad \mathbf{y} = \begin{bmatrix} u_{ind} \\ u_{inq} \\ i_{od} \\ i_{oq} \end{bmatrix} \qquad \mathbf{x} = \begin{bmatrix} i_{Ld} \\ i_{Lq} \\ u_{Cd} \\ u_{Cq} \end{bmatrix}. \tag{3.25}$$

The frequency-domain transfer functions can be solved from the time-domain state space matrices (3.23) and (3.24) by using equation

$$\mathbf{Y}(s) = \Big[\mathbf{C}(s\mathbf{I} - \mathbf{A})^{-1}\mathbf{B} + \mathbf{D}\Big]\mathbf{U}(s) = \mathbf{G}\mathbf{U}(s) \tag{3.26}$$

where s is the Laplace-variable, and $\mathbf{I}$ is the identity matrix. The transfer function matrix $\mathbf{G}$ is 4x4 matrix, where the transfer functions from current to voltage are the corresponding input impedances. Thus, the dq-domain input impedances can be extracted from $\mathbf{G}$

$$\underbrace{\begin{bmatrix} u_{ind} \\ u_{inq} \\ i_{od} \\ i_{oq} \end{bmatrix}}_{\mathbf{Y}(s)} = \underbrace{\begin{bmatrix} Z_{indd} & Z_{inqd} & \dots & \dots \\ Z_{indq} & Z_{inqq} & \dots & \dots \\ \dots & \dots & \dots & \dots \\ \dots & \dots & \dots & \dots \end{bmatrix}}_{\mathbf{G}} \underbrace{\begin{bmatrix} i_{ind} \\ i_{inq} \\ u_{od} \\ u_{oq} \end{bmatrix}}_{\mathbf{U}(s)}, \tag{3.27}$$

where the input impedances correspond to dq-domain grid impedances for circuit in Figure 3.7. The stability analysis of converters is often carried out in dq-domain, and thus the grid impedance should be in dq-domain as well. However, the state-space approach is very complex and time-consuming for larger circuits, as the size of the state matrices grows rapidly. Thus, the approach is not suitable for complex grids. However, the equation (2.16) in Section 2.4 gives the exact same result for passive circuits. This can be seen from Figure 3.8, which presents the impedance for the grid shown in Figure 3.7 with different methods, with parameters values shown in Table 3.2. In addition, the difference between impedances in different domains are shown. In conclusion, equation (2.16) is the preferred method for calculating the impedance of a grid in dq-domain.

Table 3.2 *Parameters for grid impedance calculation in dq-domain.*

Parameter	Value
R	10 Ω
L	400 μH
R_L	17.8 mΩ
C	500 μF
R_C	10 mΩ
ω_s	60 Hz

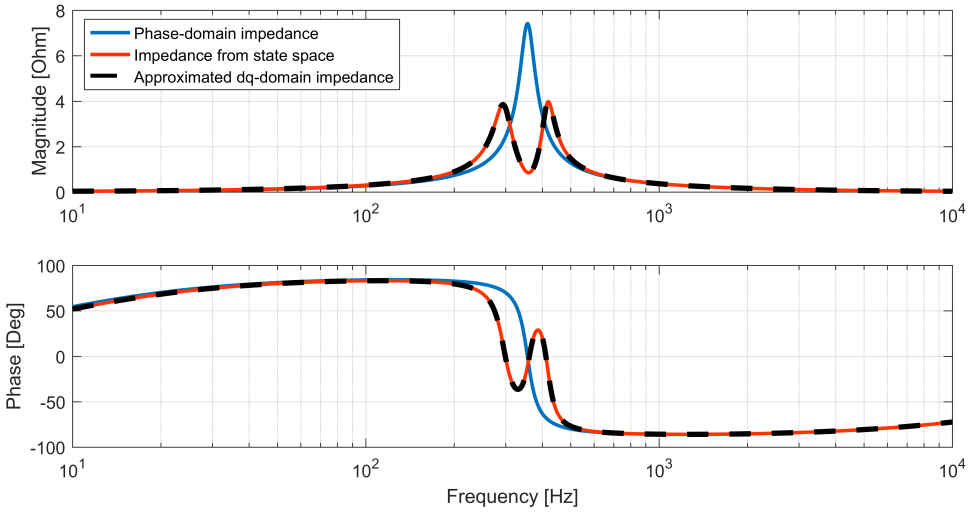

Figure 3.8 *Grid impedance with different analytical approaches.*

4. GRID EMULATION EXPERIMENTS

This chapter presents the experimental part of the thesis. First, the power hardware-in-the-loop (PHIL) method is introduced and discussed, and the experimental setup is shown. The behavior of the test setup is verified with measurements from simplified systems; the accuracy of the measurement method, real-time simulation, and grid emulation are confirmed in three separate stages. Then, the modeling methods presented in previous chapter are used for constructing models of three grid scenarios. The scenarios are then applied to the PHIL test system, and the emulated grid impedances are measured. To conclude the experimental section, the measured grid impedances are compared to analytical references and discussed thoroughly.

4.1 Power hardware-in-the-loop method

Acquiring complete hardware setup for experimental test is impractical and expensive in most of the cases. Thus, simulations are widely used for novel experiments and verification of theoretical results. However, simulations often require simplifications of real phenomena in order to achieve a usable model with reasonable computation duration. Additionally, non-linearities, parasitic elements and exact dynamic behavior are hard or impossible to model perfectly. Reduction of models causes loss of information and some phenomena may not appear in the simulated results. Therefore, measurements and experiments on real hardware are vital for final verification.

The PHIL setup combines the benefits of simulations and use of physical hardware. PHIL method adapts the use of real-time simulators and linear amplifiers connected to the hardware under testing (HUT). This setup enables easy varying of system parameters associated to the emulated system part. For example, a real inverter can be tested under different grid parameters or control schemes with no physical alterations to test setup. [56] Multiple experiments have successfully applied such PHIL methods [57, 58].

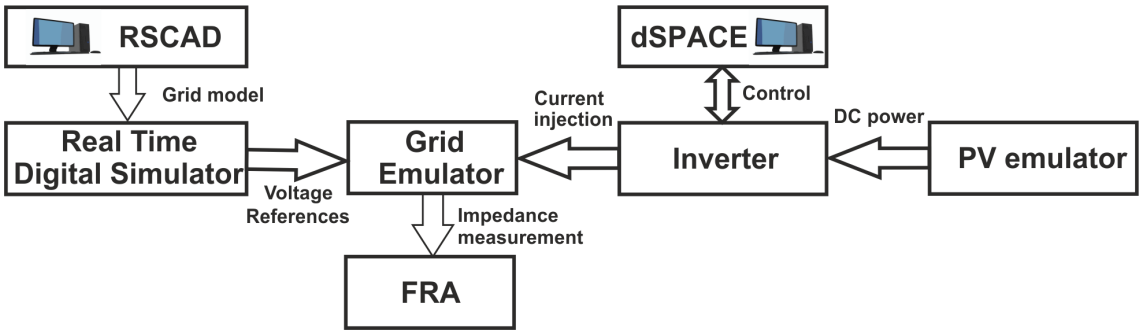

Figure 4.1 *Simplified block diagram of experimental setup.*

4.1.1 Emulation setup

In this thesis, the electrical emulation of grid impedance is based on PHIL method, where the system contains both simulation and physical hardware. Figure 4.1 depicts a simplified block diagram of the experimental setup. The main devices of the setup are real-time digital simulator (RTDS), grid emulator, inverter, and PV emulator. RTDS is used to simulate the grid model, and the simulated voltage at the point of connection is fed to grid emulator as a reference value via an optic fiber. On the other side of the setup, a PV emulator acts as a DC source for the inverter, which is further connected to the grid emulator through an LCL filter and isolation transformer. Thus, inverter fed by PV emulator is connected to an emulated grid. Therefore, the inverter can be tested in very versatile grid conditions. The focus of this thesis is on the grid emulation, and consequently the operation and control of the inverter is not thoroughly included. In order to analyze and verify the emulated grid impedances, measurements for a Venable frequency response analyzer (FRA) are connected between the grid emulator and the isolation transformer to measure the grid impedance at the point of connection. Figure 4.2 illustrates the setup in detail and includes measurement and control signals.

The PV emulator is a PVS 7000 Spitzenberger&Spies 7 kV generator, which is controlled from laboratory PC. The purpose of the emulator is to only provide the DC power for the inverter, and therefore it is set to a constant voltage and current at the MPP of a simple IV-curve. The inverter is an insulated gate bipolar transistor (IGBT) inverter model Myway Plus MWINV-9R144, which has no own control system. Instead, it is controlled using dSPACE real-time simulator running on the laboratory PC. The inverter has an output LCL filter to attenuate the harmonics in the output waveform. DC-voltage and inverter output currents and voltages are

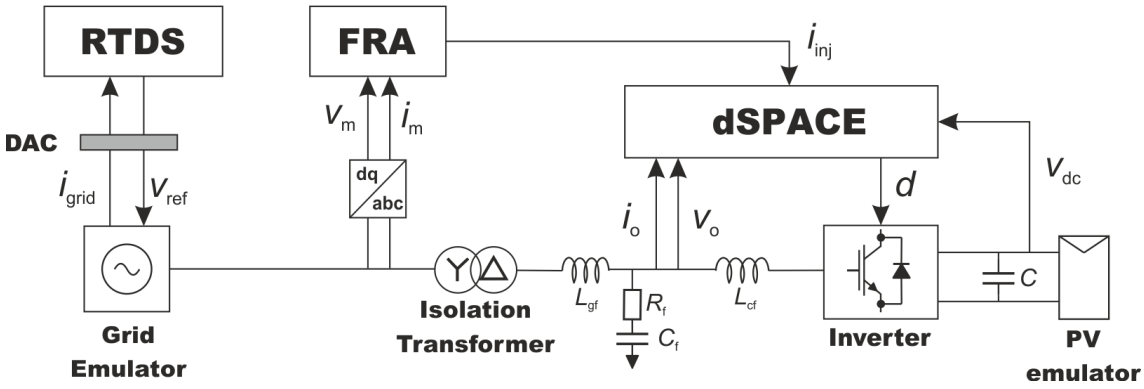

Figure 4.2 *Detailed experiment system configuration.*

measured and used in dSPACE for control implementation. The setup is designed for 120 V phase voltage and 60 Hz grid, and thus these values will be used in PHIL tests.

The grid side of the setup consists of isolation transformer, grid emulator and RTDS. The grid emulator in use is Spitzenberger&Spies PAS 15000, where three 4-quadrant linear amplifiers emulate the three-phase grid voltages based on input references. The isolation transformer must be included in order to prevent common-mode currents from damaging the setup. Thus, the grid impedance as seen from the inverter includes the series impedance of the transformer. However, as this thesis focuses on the emulation of grid, the impedance measurements are carried out from between the transformer and grid emulator. The impedance is measured using Venable FRA, which applies sinusoidal sweep over a specified frequency range. Venable injects the excitation signal to inverter output current reference which in turn includes this excitation in inverter's output current. Thus, the excitation signal is included in the current injection from the inverter. As the inverter is controlled in dq-domain, the excitation is in dq-domain as well, either to d or q-component. The frequency response (i.e. grid impedance) is derived from response signal (voltage) and injection signal (current). The response depends on the point where the measurements are taken from. As the injection is in dq-domain, the measurements are dq-transformed and, consequently the impedances are given in dq-domain. However, for passive circuits the d and q-impedances should be equal to each other. The emulated impedance is assumed to be very close to passive impedance.

The grid simulation is carried out in RTDS simulation software, RSCAD, which is specifically designed for power system simulation. The simulation is digital and the

grid emulator operates with analog signals, so the RTDS simulation is connected to grid emulator through digital-to-analog converter. Simulated voltage at the PoC is used as a reference value for grid emulator. On the other hand, simulation includes a current source, which depicts the current injected to system from the inverter. The current between the inverter and the linear amplifier is measured and fed back to RTDS after an analog-to-digital conversion as an input for the controlled current source. Thus, the emulation system is essentially a feedback system where simulator provides reference values (grid voltages) for emulator, and feedback (current measurements) is needed for accurate simulation of the grid. A digital low-pass filter is required for current measurements in order to filter out the noise [59]. The time constant is experimentally set to 15 μs, which corresponds to cut-off frequency of 10.6 kHz, for sufficient system robustness. The filtering starts to affect measurements at 1/10 of cut-off frequency, and thus the analyzed frequency range is chosen to be from 10 to 1000 Hz. The PHIL system has inherent delays, which will affect the phase at high frequencies [59].

4.2 Setup verification

Before emulating more complex power grids, the setup is tested in simplified conditions in order to verify the planned operation. In order to obtain the benefits of impedance emulation presented in Section 4.1, the grid emulation should be accurate enough. The operation is verified in three stages; first the impedance measurement system itself, then the accuracy of grid impedance simulation and emulation.

4.2.1 Measurements on physical inductors

In order to verify the proper operation of impedance measurement system, simplified tests were conducted on physical inductors. The grid emulator was set to repeat stiff voltages, and inductors with varying inductance values were connected in series before the stiff grid to operate as grid impedances. Inductors with phase inductance of 1.2 mH and 3.0 mH were used. Figure 4.3 shows the measured and calculated impedance for each case. The measurement was carried out by injecting sinusoidal excitation current to system with the inverter, and FRA was used to extract the grid impedance measurement. The impedance was measured from d-channel in the frequency range from 10 to 3000 Hz, which is identical to q-channel for passive circuits.

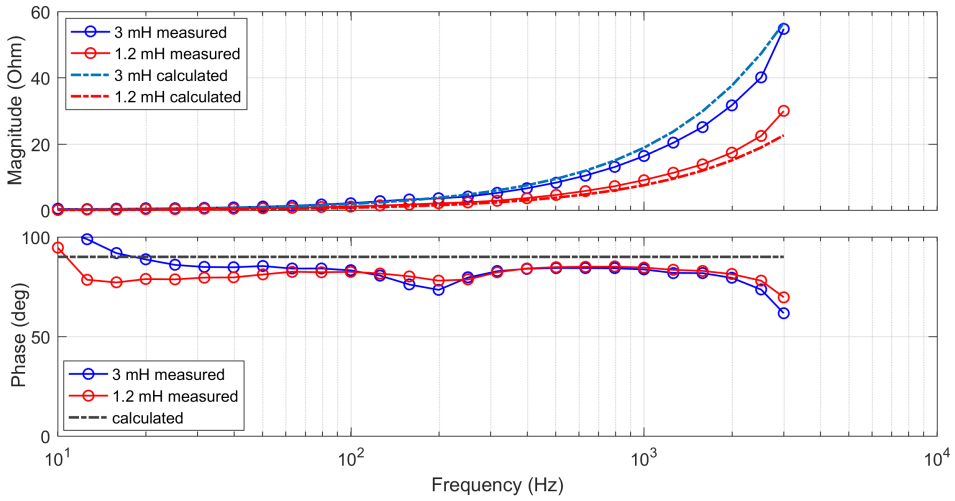

Figure 4.3 *Impedance measurements on physical inductors in comparison with analytical impedances.*

The measured magnitudes differ slightly from the analytical values, but this can be attributed mostly to inaccuracies of the real components, as the stated inductance values have margin of ±10%. Both of the measured magnitude curves appear to be within this margin. In addition, the frequency resolution was rather low in the measurement, which however should not affect results significantly. The measured phase appears to be mostly at +80-85 degrees, instead of the ideal +90 degrees. However, a real electric system always contains parasitic resistances and capacitances, and therefore the ideal phase cannot be reached in real system. Also eddy current losses in isolation transformer are increased at higher frequencies. At very low frequencies (below 20 Hz), some of the measurement values appear to be slightly above +90 degrees, which is not possible behavior for passive circuits. This is supposed to result from measurement errors, control loops of the inverter, and possible non-linearity of the grid emulator at low frequencies. The decrease of the measured phase after 1 kHz results from parasitic capacitances, which have emphasized effect at higher frequencies. As a conclusion, the comparison of measured and analytical impedance shows that the concept of impedance measurement operates as designed, and the errors resulting from measurement system are only minor. Thus, the impedance measurement based on frequency response of current injection is verified to behave as it should.

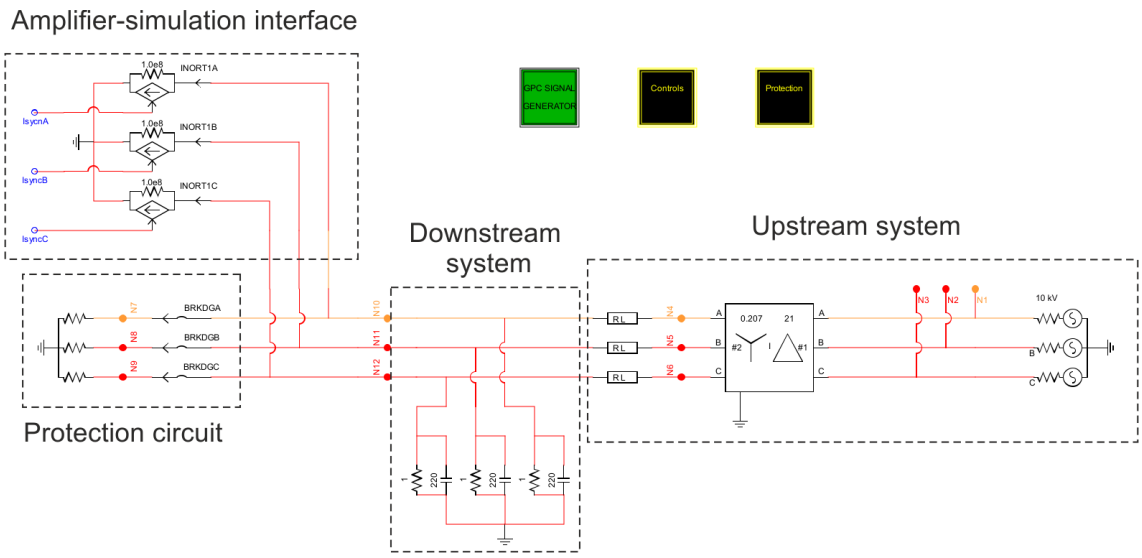

Figure 4.4 *RSCAD simulation model of a simple grid.*

4.2.2 Impedance measurements from the grid simulation

The grid impedance for the PHIL setup is simulated in a real-time simulator. The simulation model is built in RSCAD, which compiles the model for the RTDS. In order to verify the operation of the grid simulation, the impedance is measured directly from the simulator with FRA, and compared to the corresponding analytical impedance. Figure 4.4 presents the implementation of the grid simulation in RSCAD. The simulation model consists of stiff MV voltage source, transmission lines and shunt elements, and amplifier-simulation interface.

The PHIL impedance measurements are carried out in dq-domain, so the simulated impedance should be in the same domain. However, the inverter control system is responsible for dq-transformation in the complete PHIL setup. Thus, an additional dq-transformation block must be incorporated into RTDS simulation for comparable measurements, and also an implementation of phase-locked loop (PLL) is required. The increased computational burden affects the phase behavior of the impedance measurement from the simulator. Figure 4.5 shows the impedance measurement directly from the simulator in dq-domain (red), in phase domain (blue), and calculated impedance for reference (black). The magnitude of the measured impedances perfectly match the analytical values. The deviations at 60 Hz and 120 Hz origin from the fundamental frequency and dq-transformation characteristics, and are inherent in real systems. In d-channel, the phase encounters significant phase drop at higher

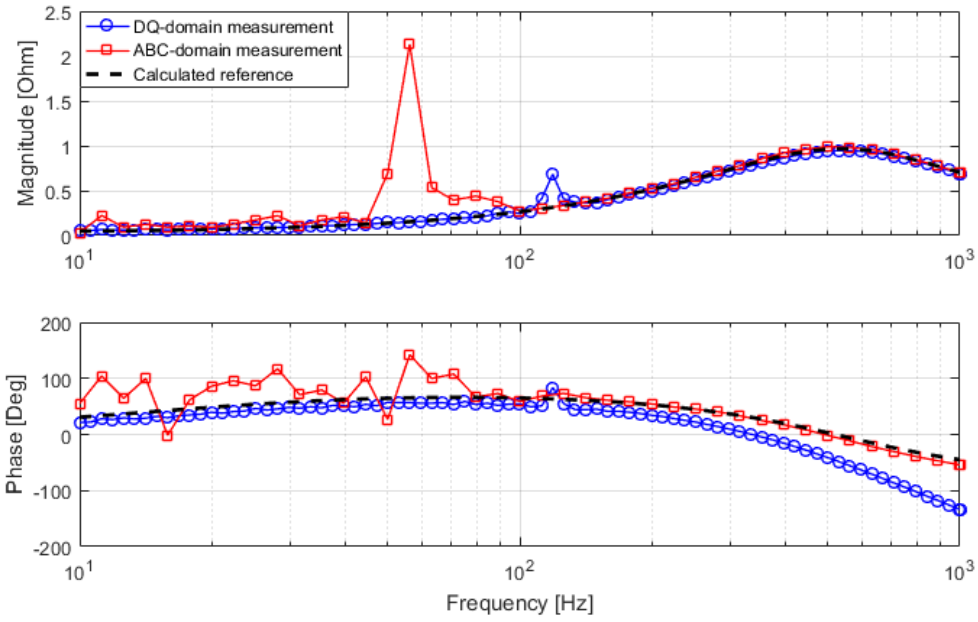

Figure 4.5 *Impedance measurements from d-channel (blue), A phase (red), and calculated reference (black).*

frequencies. For the measurement in phase domain, no additional computing is required. The measurements show large deviations below 100 Hz, but the frequency range 100-1000 Hz behaves identically with calculated impedance. Thus, the phase drop seen in dq-domain measurement results from the dq-transformation and PLL. Consequently, it can be concluded that the simulated impedance corresponds very closely to the calculated impedance, and the references for the grid emulator are correct.

4.3 Public distribution grid

This section discusses the grid impedance of a voltage distribution grid. Figure 4.6 shows the simplified grid topology for the system, which consists of MV upstream grid and local LV distribution grid, and the PoC locates in between the subsystems. The PoC could be for example the impedance seen from a grid-connected PV inverter located within the distribution system. The sub-models are derived based on Section 3.2. The distribution system consist of household customers aggregated to a distribution sub-model, which is represented by total equivalent capacitance C_{eq} and equivalent load resistance R_{eq}. On the other hand, the upstream sub-model

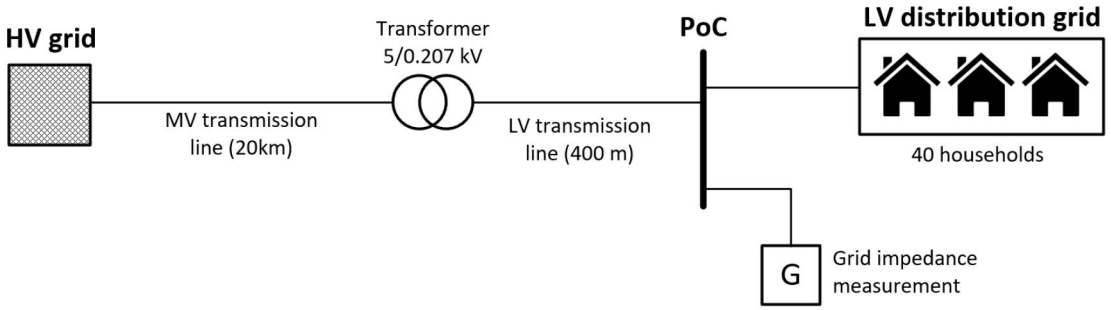

Figure 4.6 *The simplified grid model for public distribution system.*

Table 4.1 *Grid parameters for public distribution grid scenario.*

Upstream system		***Distribution system***	
Upstream voltage	5 kV	Distribution voltage	0.207 kV
Transformer reactance	11.0 %	Distribution loading	54...216 kW
Transformer resistance	1.5 %	Number of households	40
MV line length	20 km	Household capacitance	5.5 μF
MV line impedance	0.5 + j0.4 Ω/km	LV line length	0.25 km
LV line length	0.4 km	Resonant frequency	520 Hz
LV line impedance	0.4 + j0.35 Ω/km		

includes the LV and MV transmission lines and the transformer between different voltage levels. In order to account for multiple voltage levels within the system, the impedances must be reduced to the voltage level of the PoC. In this scenario, the PoC locates between sub-models, and thus they are seen as parallel connected. Table 4.1 presents the parameters used in the calculations. The analytical expression is given by equation (4.1).

$$Z_{eq} = \left(\frac{1}{R_{LV} + R'_{MV} + r_k \frac{U_{PoC}^2}{S_{tf}} + j\omega(L_{LV} + L'_{MV}) + x_k \frac{U_{PoC}^2}{S_{tf}}} + \frac{1}{R_{eq}} + j\omega C_{eq} \right)^{-1} \quad (4.1)$$

Figure 4.7 presents the grid impedances measured from the PHIL setup for two different power consumption states of the distribution grid. The impedances were measured as a sine-sweep with 400 mA current injection to system for the frequency range of 10 to 1000 Hz. The measured impedances accurately correspond to calcu-

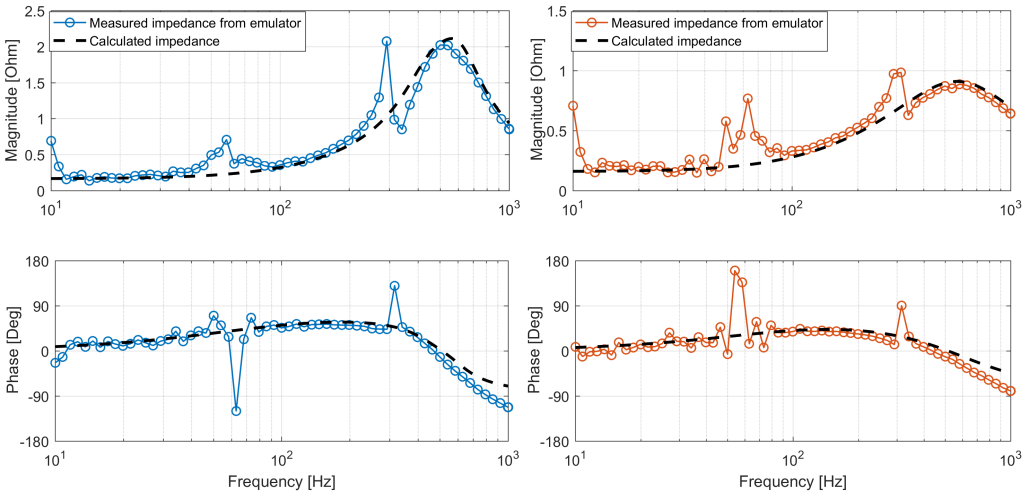

Figure 4.7 *Impedance measurements for low consumption (blue) and high consumption (red) in LV distribution system.*

lated reference, except at frequencies near 60 and 300 Hz. The deviations around 60 Hz result from the fundamental components present in the system. The deviation near 300 Hz corresponds to 5th harmonic and resembles series LC-resonance, and is most likely caused by the isolation transformer in the PHIL setup. However, the impact of the isolation transformer is not included in the scope of this thesis, and must be addressed in future works. A slight phase drop starts to occur around 400 Hz, which is caused by the delays in the system and the filtering of current measurements from the PHIL system to RTDS simulation.

The parallel resonant behavior between inductive upstream sub-model and capacitive distribution system sub-model is clearly shown as the resonance peak at 500 Hz. This is common phenomenon near consumption centers with significant equivalent capacitance. In such systems, the resonant frequency can be as low as 250 Hz [53]. With the higher power consumption (red, on right), the equivalent load resistance is smaller and thus the damping of parallel resonant circuit increases. When the power consumption decreases (blue, on left), the damping decreases and the resonance magnifies. Thus, the time-variant behavior of consumed power in customer loads causes the resonance damping to vary as well. Therefore, LC-resonant circuits may have drastic changes in the grid impedance based on season and time of the day.

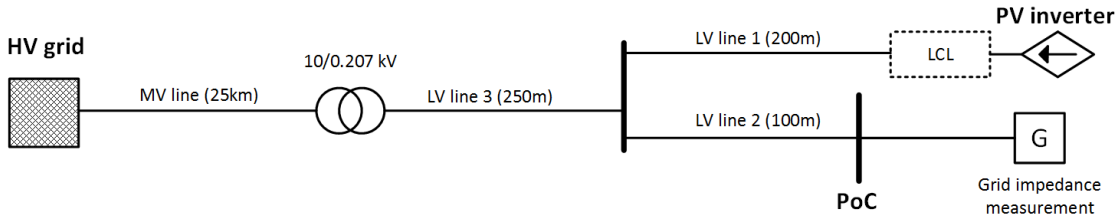

Figure 4.8 *The grid model for connection of distant PV systems.*

4.4 Remote PV plant

Figure 4.8 presents the connection of a remote large scale PV plant to grid. The unit connects to the AC grid through a single central inverter designed for 2 MW output. The voltage levels of the inverter are 207 V (AC)/500 V (DC) and the switching frequency is 5 kHz. In order to attenuate the switching effects and other adverse high-frequency noise, an LCL filter is connected between the inverter and the grid. The LV is increased to MV level for long-distance transmission in a transformer. The PoC is chosen near the transformer to correspond to the PoC of another parallel PV inverter or load center. The system can be divided to upstream and DG sub-models based on the voltage levels.

The LCL filter for the PV inverter is designed based on [38], where ratio of filter inductances is $r = 0.6$ and capacitor factor is $x = 0.05$. The equivalent impedance of the inverter is given from equations (3.9) and (3.13) in Section 3.2.3. Table 4.2 presents the resulting LCL filter parameters, inverter control parameters, and inverter equivalent impedance. The LC-resonant frequency refers to situation where the inverter is disconnected from the grid, and filter is seen as series connection of grid side inductor and filter capacitor.

The grid parameters are shown in Table 4.3. The equivalent phase-domain impedance as seen from the PoC is given by equation (4.2). For dq-domain impedance, the d-channel impedance is derived based on equation (2.16) in Section 2.4.

$$Z_{eq} = R_{LV2} + j\omega L_{LV2} + \frac{Z_u\left(R_{LV1} + j\omega L_{LV1} + j\omega L_{fg} + Z_{PV}\right)}{R_{LV1} + j\omega L_{LV1} + j\omega L_{fg} + Z_{PV} + Z_u} \tag{4.2}$$

where

Table 4.2 *LCL filter and inverter parameters for 2 MW PV inverter.*

Parameter	***Symbol***	***Value***
Filter parameters		
Grid side inductor	L_{fg}	100 μH
Converter side inductor	L_{fc}	170 μH
Filter capacitor	C_f	500 μH
Damping resistor	R_d	0.12 Ω
Filter resonant frequency	f_{res}	897 Hz
LC-resonant frequency	f_{LC}	711 Hz
Inverter control parameters		
Current controller gain	K_{CC}	$10^{42/20}$
Current controller zero	ω_{z-CC}	$2\pi350$
DC input voltage	V_{in}	700 V
Inverter equivalent impedance		
Equivalent inverter capacitance	C_{eq}	11.3 μF
Equivalent inverter resistance	R_{eq}	40.1 Ω

Table 4.3 *System parameters for impedance model of PV plant.*

Upstream system		***DG system***	
Upstream voltage	10 kV	DG system voltage	0.207 kV
Transformer reactance	10.0 %	LV line 1 length	0.2 km
Transformer resistance	1.0 %	LV line 2 length	0.1 km
Transformer power	3 MVA	LV line 3 length	0.25 km
MV line length	25 km	LV line impedance	0.1 + j0.3 Ω/km
MV line impedance	0.2 + j0.4 Ω/km		

$$Z_u = R'_{LV3} + j\omega L'_{LV3} + jx_k\frac{U_{LV}^2}{S_{tf}} + r_k\frac{U_{LV}^2}{S_{tf}} + R_{LV3} + j\omega L_{LV3} \tag{4.3a}$$

$$Z_{PV} = \frac{(R_d + \frac{1}{j\omega C_f})(j\omega L_{fc} + \frac{1}{j\omega C_{eq}} + R_{eq})}{R_d + \frac{1}{j\omega C_f} + j\omega L_{fc} + \frac{1}{j\omega C_{eq}} + R_{eq}} \tag{4.3b}$$

The grid is strongly resonant, and the measurement noise from current measurements corrupts the simulation voltages. Thus, the current low-pass filter is iteratively tuned for lower cut-off frequency. At 6.3 kHz cut-off, the main frequency

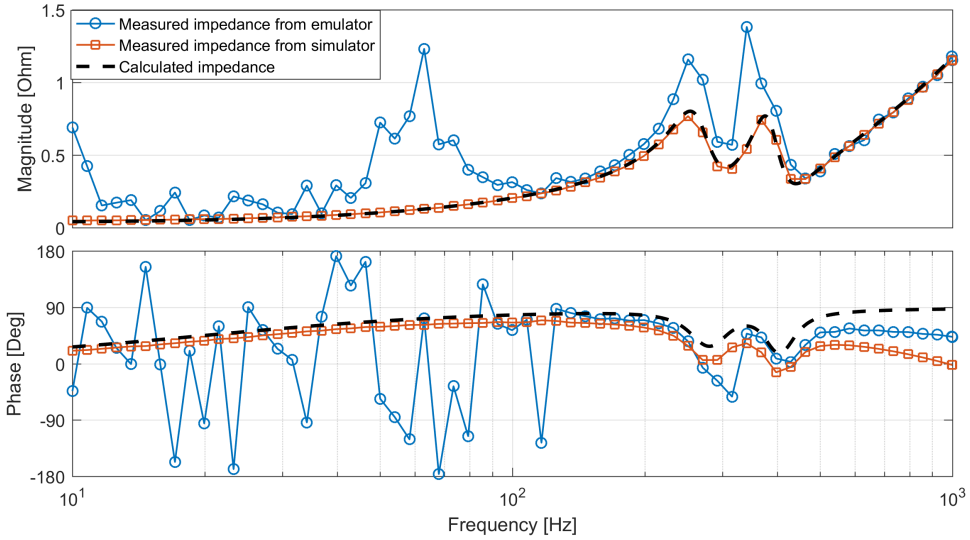

Figure 4.9 *Impedance measurements for a remote PV system from emulator (blue), simulator (red), and calculated impedance.*

component of the noise is filtered out, and the excess high-frequency ripple is removed from the grid voltages. However, this results in a further phase drop in the measurements at frequencies higher than 630 Hz. Figure 4.9 presents the impedance measurements from the RTDS simulation (blue), PHIL emulation (red), and calculated dq-domain impedance for reference (black). The impedance magnitude measurement from the simulator matches the analytically obtained impedance perfectly in the complete frequency scope. The measured phase experiences a drop due to computational delays, as discussed in Section 4.2.2. The impedance measurement from the grid emulator show similar deviations than discussed in Section 4.3. The fundamental components in the system disturb the measurements around 60 Hz. In addition, phase measurement is heavily distorted below 100 Hz, most likely due to very low grid impedance magnitude and possible non-linearities. The deviations near resonant frequency at 250-400 Hz correspond to the same frequency range than the ones observed in Section 4.3, and are most likely caused by the isolation transformer. The simulated grid topology is different, and now the resonant behavior appears to be magnified in this region. At frequencies above 400 Hz, the measured magnitude perfectly corresponds to calculated impedance. The measured phase has similar shape than in the calculated impedance, but the delays result in phase drop at high frequencies, in addition to the decreased cut-off frequency of the low-pass filter, which to decreases the phase after 600 Hz.

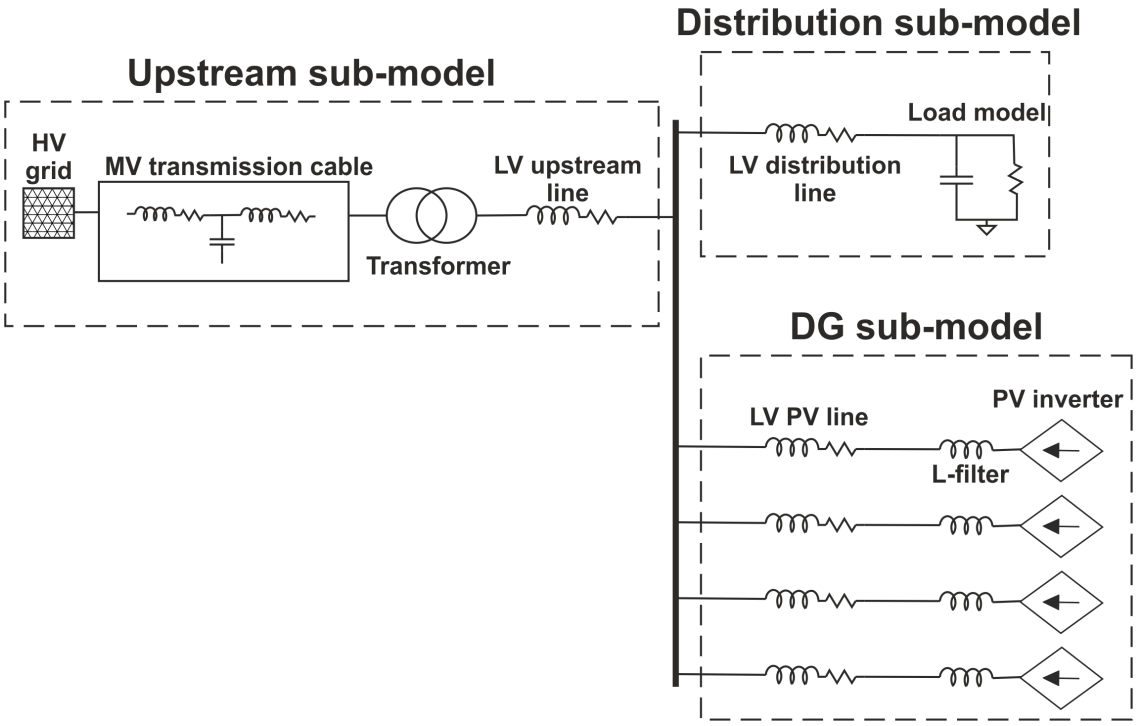

Figure 4.10 *The grid impedance model for distribution system with grid-connected PV inverters.*

4.5 Distribution system with PV generation

In this scenario, small-scale distributed generation is incorporated into a similar distribution system than in Section 4.3. Figure 4.10 presents the grid impedance model for this scenario, which consists of upstream, distribution, and DG sub-models. DG consists of 4 three-phase PV inverters with 10 kVA peak output power, located within the distribution system. The upstream transmission lines are a three-phase AHXAMK-W cable [60] and a LV overhead transmission line. A 1 MW transformer connects the systems with different voltage levels. The distribution system comprises of consumer loads (e.g. households), which are reduced to an equivalent resistance and capacitance. The PoC is located after the feeding transmission line at a bus bar.

The PV systems are connected to the AC grid through inverters with L-type output filters. The design of the filter is carried out based on [61]. The equivalent d-channel impedance for the inverter is given from equations (3.9) and (3.13) in Section 3.2.3. Table 4.4 presents the parameters for inverter and filter, and the resulting equivalent

Table 4.4 *Inverter and filter parameters for 10 kVA three-phase PV inverter.*

Parameter	***Symbol***	***Value***
Inverter and filter parameters		
Inverter switching frequency	f_{sw}	10 kHz
Current controller gain	K_{CC}	$10^{29/20}$
Current controller zero	ω_{z-CC}	$2\pi 250$ rad/s
DC input voltage	V_{in}	500 V
Output current ripple	ΔI_o	10 %
L-filter inductance	L_{fc}	2.0 mH
Inverter equivalent impedance		
Equivalent inverter capacitance	C_i	69.6 μF
Equivalent inverter resistance	R_i	8.96 Ω

Table 4.5 *Grid impedance parameters for distribution system with PV generation.*

Parameter		***Value***	***Parameter***		***Value***
MV side voltage	V_{MV}	15 kV	LV side voltage	V_{LV}	207 V
Cable length	D_c	40 km	Transformer reactance	x	8.0 %
Cable resistance	R_c	0.76 Ω/km	Transformer resistance	r	2.0 %
Cable capacitance	C_c	0.17 μF/km	Transformer power	S_{tf}	1 MW
Cable inductance	L_c	0.46 mH/km	Upstream line length	D_u	1.2 km
DG line length	D_{DG}	0.6 km	Equivalent resistance	R_{eq}	3 Ω
LV line reactance	X_l	0.35 Ω/km	Distribution line length	D_d	0.4 km
LV line resistance	R_l	0.3 Ω/km	Equivalent capacitance	C_{eq}	250 μF

impedance values for the inverter. The remaining grid impedance parameters are shown in Table 4.5.

Based on the topology shown in Figure 4.10, the equivalent impedance can be derived analytically as shown in equation (4.4). The transmission cable is analyzed as 3-cell π-model.

$$Z_{eq} = \frac{1}{\frac{1}{Z'_u} + \frac{1}{Z_d} + 4\frac{1}{Z_{PV}}} \tag{4.4}$$

where Z'_u is the upstream impedance reduced to PoC voltage level, Z_d is the dis-

tribution grid impedance, and Z_{PV} is the impedance for each PV system branch. These are given by

$$Z_u = j\omega(L_u + L_{tf} + \frac{L'_c}{3}) + (R_u + R_{tf} + \frac{R'_c}{3}) + \cfrac{1}{j\omega\frac{C'_c}{2} + \cfrac{1}{\frac{R'_c}{3} + j\omega\frac{L'_c}{3} + \cfrac{1}{j\omega\frac{C'_c}{2} + \cfrac{1}{\frac{R'_c}{3} + j\omega\frac{L'_c}{3}}}}}$$

$$Z_{PV} = j\omega(L_{fc} + L_{DG}) + R_{DG} + R_i + \frac{1}{j\omega C_i}$$

$$Z_d = j\omega L_d + R_d + \frac{1}{\frac{1}{R_{eq}} + j\omega C_{eq}}$$

Figure 4.11 presents the grid impedance measured from the simulator (red), from the grid emulator (blue), and calculated reference (black). The impedance from the simulation behaves identically than in previous measurements - perfect magnitude correspondence and delay-induced phase drop at high frequencies. The measurements from the PHIL emulation match the calculated impedance very well, with only slight deviations. The magnitude and phase follow the reference well also in frequencies below 100 Hz, except for the errors around the fundamental frequency. At 300 Hz, the same disturbance occurs than in previous measurements from the PHIL system. However, the impact is now smaller than previously observed, probably because of the more complex system and better resistive damping of resonances. The phase drop up to 45 degrees at 1 kHz is seen in the measurements. This is caused by the delays of the system, and the increased filtering between the RTDS and the linear amplifier. The methods for improving the high-frequency phase behavior of the PHIL setup are not in the scope of this thesis, but could include for example delay compensation or alternative filtering methods. However, the measurements indicate that the impedance extracted from the PHIL emulation are very accurate in general.

The shape of the impedance indicates a parallel resonance between capacitive distribution system and inductive upstream and DG submodels. The resonant behavior of the capacitive cable occurs at higher frequencies, and thus is not shown in the mea-

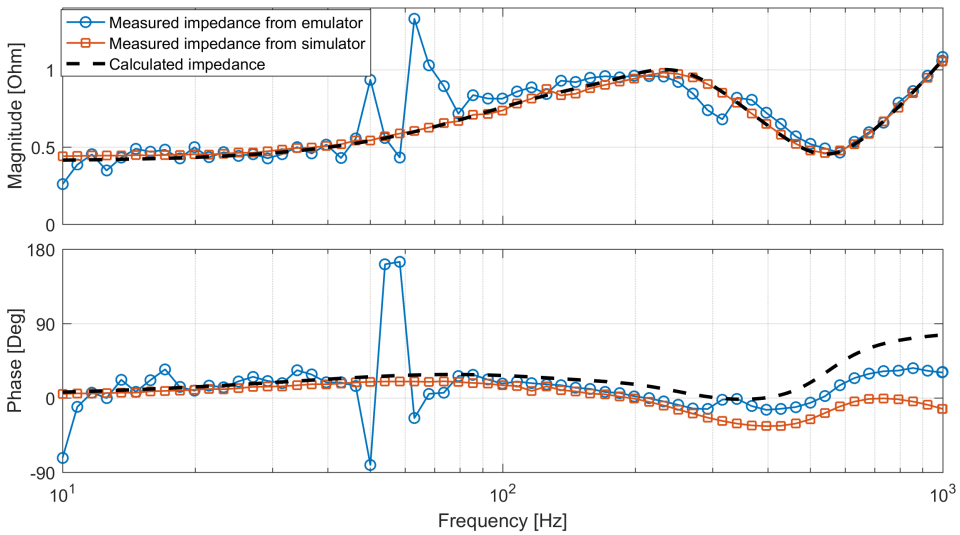

Figure 4.11 *The grid impedance measurements for distribution system with distributed small-scale PV generation.*

surements. For a grid with significant amount of DG, the design of output filters may greatly affect the grid resonances. Second-order and higher filters are resonant by nature, and could interact with capacitive and inductive elements already present in grid. This could also affect the behavior of the filter itself. However, in this scenario a simple, yet common, first-order L-filter is chosen. As the distribution sub-model introduces significant amount of capacitance into the system, LC-resonances occur. The corresponding resonant frequency can be derived based on equation (3.3) in Section 3.1.4, as shown in equation (4.6). The measurements confirm this parallel resonance around 200 Hz. As the distribution system sub-model includes a inductive transmission line, an additional series resonance occurs. Similarly to equation (4.6), the series resonant frequency is identified to be 523 Hz. At this frequency, the measurements show a dip in the impedance magnitude corresponding to series-resonant behavior. Thus, the resonances of the power system are modeled and accurately emulated to the PHIL system.

$$f_{res} = \frac{1}{2\pi\sqrt{(L_{fi} + L_{DG}) * C_{eq}}} = 199\text{Hz} \tag{4.6}$$

5. CONCLUSION

The amount of grid-connected converters in the power system is increasing at a rapid pace, driven by the progress in renewable energy technologies and in power electronics. Thus, the stability of the converter-grid interface must be analyzed carefully in order to achieve sufficient system robustness. An effective method for the stability assessment of this interface is based on the ratio of converter output impedance and the grid impedance. However, the modeling methods of the grid impedance are often insufficient, and the complex nature of the grid impedance might not be addressed adequately. The purpose of this thesis is to improve the grid impedance modeling methods to include the possible resonances and time-variances of the grid. In addition, the derived grid impedance models are used in a power hardware-in-the-loop test setup for analysis of grid-connected converters.

First, a literature survey on grid impedance modeling was carried out. The main results of the survey were that the grid impedance is often vastly simplified to a series inductance, and that the measurements on real power grids show very different results compared to the simple models. The proposed modeling is based on aggregation of grid parts into sub-models, which include the capacitive elements, and thus the resonances in the grid. Another important enhancement was the addition of time-variant loading of the grid, which may change the resonance damping dramatically.

A power hardware-in-the-loop test setup is introduced, where the grid side of the system is implemented in a real-time digital simulator. Thus, the converter can be connected to emulated grid impedance giving full control over the grid parameters. The linear amplifier acting as a grid emulator provides the grid voltage for a grid-connected photovoltaic inverter. The grid impedance was measured with a sine sweep from both the pure simulation, and grid emulation, in the frequency range from 10 to 1000 Hz. The comparison of the analytical grid impedance to the impedance measured from the emulator showed the emulation to resemble the shape

of the impedance accurately. Inaccuracies at low frequencies and near fundamental frequency were very likely caused by the measurement methods instead of errors in the emulation. The emulated impedance deviated from the reference at around 300 Hz, which results most likely from the isolation transformer located in between the grid emulator and the inverter. At higher frequencies (above 500 Hz), the phase starts to drop from the reference. This is caused by the delays in the system and the filtering.

As the available impedance measurement data is scarce, the applied methods for grid impedance modeling have their limitations. For example, the consumer loads were aggregated into an equivalent capacitance and resistance instead of more precise complex model, as reliable information on the real impedance of an average household was not available. Regardless, the proposed models provide vast improvements over the most commonly used even simpler models. On the other hand, the impedance emulation is limited by the required filtering of current measurements, the delays of the systems, and possible limitations imposed by the interfacing algorithms. However, the interfacing of the emulator and the simulation is out of the scope for this thesis. Although the models and the test setup have limitations, they still provide very effective tools for more accurate stability assessment of the converter-grid interface.

This thesis suggests considering the use of aggregated grid impedance models for stability and control assessments when the grid impedance is an important parameter. Especially the possibility of resonance and time-variance of the grid impedance should be considered. The real-time simulation can effortlessly produce varying grid conditions, which would be practically impossible to implement with hardware only. The impedance of the emulation accurately corresponds to the reference simulation, and thus the analysis of converters can be done cost-effectively even in complex systems. On the other hand, the use of real hardware in the converter side diminishes the need for complicated modeling of converter dynamics. In conclusion, the PHIL test setup proved to be a very effective and versatile tool for analysis of grid-connected converters.

The future topics related to this work include for example

1. increasing the complexity and thus the accuracy of the grid simulation
2. introducing real-time changes to the simulated grid impedance

3. assessing the system behavior during system transients, e.g. faults
4. comparing and implementing different interfacing algorithms for emulation
5. addressing the issues related to multiple parallel-connected inverters
6. adaptive control of grid-connected converters.

The impedance models and the PHIL setup introduced in this thesis will be the foundation for Author's doctoral studies, which will focus on the stability assessment of parallel inverters in large-scale power systems.

BIBLIOGRAPHY

[1] European Commission, "Energy 2020: A strategy for competitive, sustainable and secure energy," 2011.

[2] B. K. Bose, "Global energy scenario and impact of power electronics in 21st century," *IEEE Transactions on Industrial Electronics*, vol. 60, no. 7, pp. 2638–2651, 2013.

[3] Y. Tang, L. Huang, and G. Zhao, "Resonant feed forward control for LCL-type grid-tied inverters in weak grid condition," in *2016 IEEE Energy Conversion Congress and Exposition (ECCE)*, 2016, pp. 1–6.

[4] S. Zhang, S. Jiang, and X. Lu, "Resonance issues and damping techniques for grid-connected inverters with long transmission cable," *IEEE Transactions on Power Electronics*, vol. IEEE Transactions on Power Electronics, no. 1, p. 110, 2014.

[5] R. Luhtala, "Adaptive control of grid-connected inverters," 2017, Master's thesis, Tampere University of Technology.

[6] J. A. Suul, S. D'Arco, P. Rodriguez, and M. Molinas, "Impedance-compensated grid synchronisation for extending the stability range of weak grids with voltage source converters," *IET Generation, Transmission & Distribution*, vol. 10, no. 6, pp. 1315–1326, 2016.

[7] T. Su, W. Liu, Y. Wang, J. Sun, and X. Zha, "A composite compensation method of a grid-connected AC/DC converter to improve robustness under weak grid conditions," in *2015 IEEE Energy Conversion Congress and Exposition (ECCE)*, 2015, pp. 6853–6857.

[8] C. Buchhagen, C. Rauscher, A. Menze, and J. Jung, "Borwin1 - first experiences with harmonic interactions in converter dominated grids," in *International ETG Congress 2015; Die Energiewende - Blueprints for the new energy age*, 2015, pp. 1–7.

[9] C. Li, "Unstable operation of photovoltaic inverter from field experiences," *IEEE Transactions on Power Delivery*, vol. PP, no. 99, pp. 1–1, 2017.

[10] G. D. Irwin, A. K. Jindal, and A. L. Isaacs, "Sub-synchronous control interactions between type 3 wind turbines and series compensated AC transmission systems," in *2011 IEEE Power and Energy Society General Meeting*, 2011, pp. 1–6.

[11] S. L. Lorenzen, A. B. Nielsen, and L. Bede, "Control of a grid connected converter during weak grid conditions," in *2016 IEEE 7th International Symposium on Power Electronics for Distributed Generation Systems (PEDG)*, 2016, pp. 1–6.

[12] Q. Zhao, H. Zhang, W. Song, X. Li, and Q. Yang, "Regulator reconstruction strategy of grid-connected inverter in weak grid," in *2016 IEEE 8th International Power Electronics and Motion Control Conference (IPEMC-ECCE Asia)*, 2016, pp. 451–457.

[13] D. Yang, X. Ruan, and H. Wu, "Impedance shaping of the grid-connected inverter with LCL filter to improve its adaptability to the weak grid condition," *IEEE Transactions on Power Electronics*, vol. 29, no. 11, pp. 5795–5805, 2014.

[14] D. Yang, X. Wang, F. Liu, K. Xin, Y. Liu, and F. Blaabjerg, "Adaptive reactive power control of PV power plants for improved power transfer capability under ultra-weak grid conditions," *IEEE Transactions on Smart Grid*, vol. PP, no. 99, pp. 1–1, 2017.

[15] Q. Yang, K. Li, C.-M. Zhao, and H. Wang, "The resonance suppression for parallel photovoltaic grid-connected inverters in weak grid," *International Journal of Automation and Computing*, 05/24 2017. [Online]. Available: https://doi.org/10.1007/s11633-017-1072-0

[16] X. Chen, J. Chen, C. Gong, and H. Wang, "Impedance-based analysis of grid-connected inverter in high impedance grids," in *2013 IEEE 8th Conference on Industrial Electronics and Applications (ICIEA)*, 2013, pp. 1284–1289.

[17] A. Etxegarai, P. Eguia, E. Torres, A. Iturregi, and V. Valverde, "Review of grid connection requirements for generation assets in weak power grids," *Renewable and Sustainable Energy Reviews*, vol. 41, pp. 1501–1514, 2015.

[18] T. Midtsund, J. A. Suul, and T. Undeland, "Evaluation of current controller performance and stability for voltage source converters connected to a weak grid," in *The 2nd International Symposium on Power Electronics for Distributed Generation Systems*, 2010, pp. 382–388.

[19] J. J. Sun, W. Hu, H. Zhou, Y. M. Jiang, and X. M. Zha, "A resonant characteristics analysis and suppression strategy for multiple parallel grid-connected inverters with LCL filter," *Journal of power electronics*, vol. 16, pp. 1483–1493, 2016.

[20] M. Liserre, R. Teodorescu, and F. Blaabjerg, "Stability of photovoltaic and wind turbine grid-connected inverters for a large set of grid impedance values," *IEEE Transactions on Power Electronics*, vol. 21, no. 1, pp. 263–272, 2006.

[21] Y. A. R. I. Mohamed, "Suppression of low- and high-frequency instabilities and grid-induced disturbances in distributed generation inverters," *IEEE Transactions on Power Electronics*, vol. 26, no. 12, 2011.

[22] M. Lu, A. Al-Durra, S. M. Muyeen, S. Leng, P. C. Loh, and F. Blaabjerg, "Benchmarking of stability and robustness against grid impedance variation for LCL-filtered grid-interfacing inverters," *IEEE Transactions on Power Electronics*, no. 99, pp. 1–1, 2017.

[23] J. Sun, "Impedance-based stability criterion for grid-connected inverters," *IEEE Transactions on Power Electronics*, vol. 26, no. 11, pp. 3075–3078, 2011.

[24] T. Roinila, M. Vilkko, and J. Sun, "Broadband methods for online grid impedance measurement," in *2013 IEEE Energy Conversion Congress and Exposition*, 2013, pp. 3003–3010.

[25] M. Liserre, F. Blaagjerg, and R. Teodorescu, "Grid impedance detection via excitation of LCL-filter resonance," in *Fourtieth IAS Annual Meeting. Conference Record of the 2005 Industry Applications Conference, 2005.*, vol. 2, 2005, pp. 910–916 Vol. 2.

[26] S. Gunter, F. W. Fuchs, and H.-J. Hinrichs, "A method to measure the network harmonic impedance," *PCIM Europe 2013, Nuremberg*, 2013.

[27] Y. A. Familiant, J. Huang, K. A. Corzine, and M. Belkhayat, "New techniques for measuring impedance characteristics of three-phase AC power systems," *IEEE Transactions on Power Electronics*, vol. 24, no. 7, pp. 1802–1810, 2009.

[28] M. Jordan, H. Langkowski, T. D. Thanh, and D. Schulz, "Frequency dependent grid-impedance determination with pulse-width-modulation-signals," in *2011 7th International Conference-Workshop Compatibility and Power Electronics (CPE)*, 2011, pp. 131–136.

[29] A. Knop and F. W. Fuchs, "High frequency grid impedance analysis by current injection," in *2009 35th Annual Conference of IEEE Industrial Electronics*, 2009, pp. 536–541.

[30] L. Jessen, S. Gunter, F. W. Fuchs, M. Gottschalk, and H. J. Hinrichs, "Measurement results and performance analysis of the grid impedance in different low voltage grids for a wide frequency band to support grid integration of renewables," in *2015 IEEE Energy Conversion Congress and Exposition (ECCE)*, 2015, pp. 1960–1967.

[31] L. Jessen and F. W. Fuchs, "Investigation of renewable energy generation and load impact on the grid impedance at different points of connection in public low voltage grids to support grid integration of renewable energies," in *2016 18th European Conference on Power Electronics and Applications (EPE'16 ECCE Europe)*, 2016, pp. 1–10.

[32] S. Grunau, J. Reese, L. Jessen, and F. W. Fuchs, "Aspects of grid integration of renewable energy sources in weak power systems," in *International ETG-Congress 2013; Symposium 1: Security in Critical Infrastructures Today*, 2013, pp. 1–7.

[33] J. Xie, Y. Feng, and N. Krap, "Network impedance measurements for three-phase high-voltage power systems," in *Power and Energy Engineering Conference (APPEEC)*. IEEE Xplore, 2010.

[34] T. Suntio, T. Messo, and J. Puukko, *Power Electronic Converters - Dynamics and Control in Conventional and Renewable Energy Applications*. Wiley-VCH, 11 2017.

[35] J. Ribrant and L. Bertling, "Survey of failures in wind power systems with focus on Swedish wind power plants during 1997-2005," in *2007 IEEE Power Engineering Society General Meeting*, 2007, pp. 1–8.

[36] R. Burgos, D. Boroyevich, F. Wang, K. Karimi, and G. Francis, "On the AC stability of high power factor three-phase rectifiers," in *2010 IEEE Energy Conversion Congress and Exposition*, 2010, pp. 2047–2054.

[37] R. D. Middlebrook, "Input filter considerations in design and application of switching regulators," *IEEE Ind. Appl. Soc. Annu. Meeting*, p. 366, 1976.

[38] M. Liserre, F. Blaabjerg, and S. Hansen, "Design and control of an LCL-filter based three-phase active rectifier," in *Conference Record of the 2001 IEEE Industry Applications Conference. 36th IAS Annual Meeting (Cat. No.01CH37248)*, vol. 1, 2001, pp. 299–307 vol.1.

[39] L. Asiminoaei, R. Teodorescu, F. Blaabjerg, and U. Borup, "A digital controlled PV-inverter with grid impedance estimation for ENS detection," *IEEE Transactions on Power Electronics*, vol. 20, no. 6, pp. 1480–1490, 2005.

[40] A. V. Timbus, R. Teodorescu, and P. Rodriguez, "Grid impedance identification based on active power variations and grid voltage control," in *2007 IEEE Industry Applications Annual Meeting*, 2007, pp. 949–954.

[41] S. Marx and D. Bender, "An introduction to symmetrical components, system modeling and fault calculation," in *31th Annual. HANDS-ON Relay School*, Washington, 2014.

[42] European Standard, "EN 50160: Voltage characteristics of electricity supplied by public distribution systems," 1999.

[43] T. M. Shoemaker and J. E. Mack, *Chapter 15: Distribution Transformers*, 11th ed., ser. The Lineman's and Cableman's Handbook. McGraw-Hill, 2002.

[44] J. Elovaara and L. Haarla, *Sahkoverkot 1 - Jarjestelmatekniikka ja sahkoverkon laskenta*, 2nd ed. Otetieto, 2011.

[45] J. W. Feltes and B. S. Fernandes, "Wind turbine generator dynamic performance with weak transmission grids," in *2012 IEEE Power and Energy Society General Meeting*, 2012, pp. 1–7.

[46] N. Strachan and D. Dragan, "Stability of a variable speed permanent magnet wind generator with weak AC grids," *IEEE Transactions of Power Delivery*, 2010.

[47] L. D. Aguiar, R. Cardoso, C. Stein, P. D. Costa, and E. Carati, *Distributed Renewable Power Sources in Weak Grids - Analysis and Control.* Intechopen, 05/11 2016.

[48] Z. J. Z, "Impact of short circuit ratio and phase locked loop parameters on the small-signal behaviour of a VSC-HVDC converter," in *2016 IEEE Power and Energy Society General Meeting (PESGM)*, 2016, pp. 1–1.

[49] J. Xu, B. Zhang, Q. Qian, X. Meng, and S. Xie, "Robust control and design based on impedance-based stability criterion for improving stability and harmonics rejection of inverters in weak grid," in *2017 IEEE Applied Power Electronics Conference and Exposition (APEC)*, 2017, pp. 3619–3624.

[50] S. Grunau and F. W. Fuchs, "Effect of wind-energy power injection into weak grids," *European Wind Energy Conference and Exhibition 2012, EWEC 2012*, vol. 2, pp. 1150–1156, 01/01 2012.

[51] M. Davari and Y. A. R. I. Mohamed, "Robust vector control of a very weak-grid-connected voltage-source converter considering the phase-locked loop dynamics," *IEEE Transactions on Power Electronics*, vol. 32, no. 2, pp. 977–994, Feb 2017.

[52] X. Wang, D. Yang, and F. Blaabjerg, "Harmonic current control for LCL-filtered VSCs connected to ultra-weak grids," in *2017 IEEE Energy Conversion Congress and Exposition (ECCE)*, Oct 2017, pp. 1608–1614.

[53] J. H. R. Enslin and P. J. M. Heskes, "Harmonic interaction between a large number of distributed power inverters and the distribution network," *IEEE Transactions on Power Electronics*, vol. 19, no. 6, pp. 1586–1593, 2004.

[54] N. Espinoza, M. Bongiorno, and O. Carlson, "Frequency characterization of type-IV wind turbine systems," in *2016 IEEE Energy Conversion Congress and Exposition (ECCE)*, 2016, pp. 1–8.

[55] L. Jessen and F. W. Fuchs, "Modeling of inverter output impedance for stability analysis in combination with measured grid impedances," in *2015 IEEE 6th International Symposium on Power Electronics for Distributed Generation Systems (PEDG)*, 2015, pp. 1–7.

[56] P. C. Kotsampopoulos, F. Lehfuss, G. F. Lauss, B. Bletterie, and N. D. Hatziargyriou, "The limitations of digital simulation and the advantages of PHIL testing in studying distributed generation provision of ancillary services," *IEEE Transactions on Industrial Electronics*, vol. 62, no. 9, pp. 5502–5515, 2015.

[57] T. Reinikka, "Implementation of online impedance measurement setup for three-phase grid-connected inverters," 2017, Master's thesis, Tampere University of Technology.

[58] T. Messo, J. Sihvo, T. Roinila, and R. Luhtala, "Hardware-in-the-loop emulation of three-phase grid impedance for characterizing impedance-based instability," in *2016 9th EUROSIM Congress on Modelling and Simulation*, 2016.

[59] S. Lentijo, S. D'Arco, and A. Monti, "Comparing the dynamic performances of power hardware-in-the-loop interfaces," *IEEE Transactions on Industrial Electronics*, vol. 57, no. 4, pp. 1195–1207, 2010.

[60] Prysmian group, "AHXAMK-W 20 kv 3-johtiminen alumiinijohtiminen, PEX-eristeinen vesitiivis Wiski-maakaapeli," 2018.

[61] K. H. Ahmed, S. J. Finney, and B. W. Williams, "Passive filter design for three-phase inverter interfacing in distributed generation," in *2007 Compatibility in Power Electronics*, 2007, pp. 1–9.

APPENDIX A: SMALL-SIGNAL STATE SPACE OF A VOLTAGE-FED INVERTER

This section shows the construction of small-signal dynamic model of a three-phase voltage-fed inverter. The aim is to achieve the transfer functions for open-loop in dq-domain.

First, the equations for inductor voltages must be constructed for both states of switch. This results in

$$\begin{bmatrix} v_{La}^{P} \\ v_{Lb}^{P} \\ v_{Lc}^{P} \end{bmatrix} = \begin{bmatrix} v_{in} \\ v_{in} \\ v_{in} \end{bmatrix} - (r_{ds} + r_L) * \begin{bmatrix} i_{La} \\ i_{Lb} \\ i_{Lc} \end{bmatrix} - \begin{bmatrix} v_{an} \\ v_{bn} \\ v_{cn} \end{bmatrix} - \begin{bmatrix} v_{nN} \\ v_{nN} \\ v_{nN} \end{bmatrix} \tag{1}$$

for positive switching time for each leg, where indexes a, b, and c refer to phase. For negative switching time the equations are similar, but instead of input voltage, the switch connects each leg into neutral

$$\begin{bmatrix} v_{La}^{N} \\ v_{Lb}^{N} \\ v_{Lc}^{N} \end{bmatrix} = -(r_{ds} + r_L) * \begin{bmatrix} i_{La} \\ i_{Lb} \\ i_{Lc} \end{bmatrix} - \begin{bmatrix} v_{an} \\ v_{bn} \\ v_{cn} \end{bmatrix} - \begin{bmatrix} v_{nN} \\ v_{nN} \\ v_{nN} \end{bmatrix}. \tag{2}$$

The voltage over an inductor corresponds to the time-derivative of inductor current. Thus when averaging over a switching cycle using duty ratio d_i we can solve the averaged inductor current derivatives

$$\frac{d}{dt} \begin{bmatrix} \langle i_{La} \rangle \\ \langle i_{Lb} \rangle \\ \langle i_{Lc} \rangle \end{bmatrix} = \frac{1}{L} \left(\begin{bmatrix} d_a \\ d_b \\ d_c \end{bmatrix} * \langle v_{in} \rangle - (r_{ds} + r_l) * \begin{bmatrix} \langle i_{La} \rangle \\ \langle i_{Lb} \rangle \\ \langle i_{Lc} \rangle \end{bmatrix} - \begin{bmatrix} \langle v_{an} \rangle \\ \langle v_{bn} \rangle \\ \langle v_{cn} \rangle \end{bmatrix} - \begin{bmatrix} \langle v_{nN} \rangle \\ \langle v_{nN} \rangle \\ \langle v_{nN} \rangle \end{bmatrix} \right) \tag{3}$$

where brackets denote the averaged value of each quantity and d is duty ratio of each switch. Next, the inductor current equation is transformed to dq-domain using Park matrix presented in 2.1.1. Zero sequence components are neglected, as there is no path for them.

$$\frac{d\langle i_{Ld} \rangle}{dt} = \frac{1}{L} \Big(d_d \langle v_{in} \rangle + \omega_s L \langle i_{Lq} \rangle - (r_{ds} + r_L) \langle i_{Ld} \rangle - \langle v_{od} \rangle \Big) \tag{4}$$

$$\frac{d\langle i_{Lq}\rangle}{dt} = \frac{1}{L}\Big(d_q\langle v_{in}\rangle - \omega_s L\langle i_{Ld}\rangle - (r_{ds}+r_L)\langle i_{Lq}\rangle - \langle v_{oq}\rangle\Big) \tag{5}$$

The cross-couplings locate to terms $\omega_s L\langle i_{Lq}\rangle$ and $-\omega_s L\langle i_{Ld}\rangle$ in these equations. The output currents equal to inductor currents in each phase for both components, and the input current is

$$\langle i_{in}\rangle = \frac{3}{2}\Big(d_d\langle i_{Ld}\rangle + d_q\langle i_{Lq}\rangle\Big) \tag{6}$$

$$\langle i_{od}\rangle = \langle i_{Ld}\rangle \tag{7}$$

$$\langle i_{oq}\rangle = \langle i_{Lq}\rangle \tag{8}$$

Linearizing the average model by solving first-order partial derivatives for each variable yields linearized state-space

$$\frac{d\langle i_{Ld}\rangle}{dt} = -\frac{r_{ds}+r_L}{L}\,\hat{i}_{Ld} + \omega_s\hat{i}_{Lq} + \frac{D_d}{L}\hat{v}_{in} - \frac{1}{L}\hat{v}_{od} + \frac{V_{in}}{L}\hat{d}_d \tag{9}$$

$$\frac{d\langle i_{Lq}\rangle}{dt} = -\frac{r_{ds}+r_L}{L}\,\hat{i}_{Lq} + \omega_s\hat{i}_{Ld} + \frac{D_q}{L}\hat{v}_{in} - \frac{1}{L}\hat{v}_{oq} + \frac{V_{in}}{L}\hat{d}_q \tag{10}$$

$$\hat{i}_{in} = \frac{3D_d}{2}\hat{i}_{Ld} + \frac{3D_q}{2}\hat{i}_{Lq} + \frac{3I_{Ld}}{2}\hat{d}_d + \frac{3I_{Lq}}{2}\hat{d}_q \tag{11}$$

$$\hat{i}_{od} = \hat{i}_{Ld} \tag{12}$$

$$\hat{i}_{oq} = \hat{i}_{Lq} \tag{13}$$

where capital letters denote steady state constant values and variables with hat are linearized values. Linearized state-space can be denoted in matrix form

$$\frac{\mathrm{d}}{\mathrm{d}t}\mathbf{x} = \underbrace{\begin{bmatrix} -\frac{r_{ds}+r_L}{L} & \omega_s \\ -\omega_s & -\frac{r_{ds}+r_L}{L} \end{bmatrix}}_{\mathbf{A}}\mathbf{x} + \underbrace{\begin{bmatrix} -\frac{1}{L} & 0 & \frac{D_d}{L} & \frac{V_{in}}{L} & 0 \\ 0 & \frac{1}{L} & \frac{D_q}{L} & 0 & \frac{V_{in}}{L} \end{bmatrix}}_{\mathbf{B}}\mathbf{u} \tag{14}$$

$$\mathbf{y} = \underbrace{\begin{bmatrix} \frac{3D_d}{2} & \frac{3D_q}{2} \\ 1 & 0 \\ 0 & 1 \end{bmatrix}}_{\mathbf{C}}\mathbf{x} + \underbrace{\begin{bmatrix} 0 & 0 & 0 & \frac{3I_{Ld}}{2} & \frac{3I_{Lq}}{2} \\ 0 & 0 & 0 & 0 & 0 \\ 0 & 0 & 0 & 0 & 0 \end{bmatrix}}_{\mathbf{D}}\mathbf{u} \tag{15}$$

where input ($\mathbf{u}$), output ($\mathbf{y}$) and state ($\mathbf{x}$) variable vectors are

$$\mathbf{x} = \begin{bmatrix} \hat{i}_{Ld} \\ \hat{i}_{Lq} \end{bmatrix} \qquad \mathbf{u} = \begin{bmatrix} \hat{v}_{od} \\ \hat{v}_{oq} \\ \hat{v}_{in} \\ \hat{d}_d \\ \hat{d}_q \end{bmatrix} \qquad \mathbf{y} = \begin{bmatrix} \hat{i}_{in} \\ \hat{i}_{od} \\ \hat{i}_{oq}. \end{bmatrix} \tag{16}$$

Laplace transform on state-space matrix transforms it to the frequency domain according to

$$\mathbf{Y}(s) = \mathbf{G}\mathbf{U}(s) = [\mathbf{C}(s\mathbf{I} - \mathbf{A})^{-1}\mathbf{B}]\mathbf{U}(s) \tag{17}$$

where $\mathbf{I}$ is identity matrix and $\mathbf{G}$ represents the input-to-output transfer function matrix consisting of 3 x 5 open-loop transfer functions. The transfer functions for open-loop are

$$\underbrace{\begin{bmatrix} \hat{i}_{in} \\ \hat{i}_{od} \\ \hat{i}_{oq} \end{bmatrix}}_{\mathbf{y}} = \underbrace{\begin{bmatrix} T_{oid-o} & T_{oiq-o} & Y_{in-o} & G_{cid-o} & G_{ciq-o} \\ -Y_{odd-o} & -Y_{oqd-o} & G_{iod-o} & G_{codd-o} & G_{coqd-o} \\ -Y_{odq-o} & -Y_{oqq-o} & G_{ioq-o} & G_{codq-o} & G_{coqq-o} \end{bmatrix}}_{\mathbf{G}} \underbrace{\begin{bmatrix} \hat{v}_{od} \\ \hat{v}_{oq} \\ \hat{v}_{in} \\ \hat{d}_d \\ \hat{d}_q \end{bmatrix}}_{\mathbf{u}} \tag{18}$$